



A Direct Simulation Monte Carlo–Driven Photochemical Model of Callisto’s Ionosphere

Shane R. Carberry Mogan^{1,3} , Luke E. Moore² , Lucas Liuzzo¹ , and Andrew R. Poppe¹

¹ Space Sciences Laboratory, University of California, Berkeley, CA, USA

² Center for Space Physics, Boston University, Boston, MA, USA

Received 2024 December 12; revised 2025 March 6; accepted 2025 March 24; published 2025 May 2

Abstract

Here we present a photochemical model of Callisto’s ionosphere with inputs supplied by a direct simulation Monte Carlo model of its neutral atmosphere. We compare a model that considers interactions with photons as the sole external ionization mechanism to models also including magnetospheric electron impacts, where upstream electron densities and temperatures are varied over an order of magnitude to constrain the role that the highly variable electron population near Callisto has on the underlying ionospheric structure. Depending on the implemented upstream electron density, magnetospheric electron impacts dominate the production of Callisto’s ionosphere or induce reactions at rates comparable to or less than those from solar photons. Furthermore, depending on the implemented upstream electron temperature, electron impacts either preferentially dissociate or ionize molecules. We show that ionization of an O₂ component with a surface number density of 10⁹ cm⁻³, which is consistent with recent remote observations and models, is capable of producing the electron densities detected during Galileo radio occultations, from which an O₂ surface density of ~10¹⁰ cm⁻³ was initially inferred. The modeled total plasma densities are also compared to those inferred from Galileo plasma-wave measurements and yield a reasonable agreement up to ~1000 km, presenting the first model capable of simultaneously producing both Galileo radio occultations and plasma-wave observations. Finally, the implications of this work are discussed, highlighting several leads that need to be explored going forward to better constrain Callisto’s atmosphere, ionosphere, and local plasma environment in anticipation of the eventual Jupiter Icy Moons Explorer observations.

Unified Astronomy Thesaurus concepts: Exosphere (499); Callisto (2279); Galilean satellites (627); Planetary science (1255); Planetary atmospheres (1244); Planetary ionospheres (2185); Ionization (2068); Photoionization (2060); Electron impact ionization (2059); Natural satellite atmospheres (2214); Jovian satellites (872); Planetary magnetospheres (997)

1. Introduction

Callisto, the outermost Galilean satellite of Jupiter, possesses a coupled atmosphere–ionosphere system, the formation of which is the result of physical and chemical processes induced by the impinging, corotating Jovian magnetospheric plasma and solar irradiation. Callisto’s atmosphere is predominantly composed of molecules produced via radiolysis in the icy regolith from which they subsequently release—CO₂ (R. W. Carlson 1999; R. J. Cartwright et al. 2024), O₂ (N. J. Cunningham et al. 2015; S. R. Carberry Mogan et al. 2023a; K. de Kleer et al. 2023), and H₂ (S. R. Carberry Mogan et al. 2022)—as well as trace species produced via dissociative processes in the atmosphere, namely, O (N. J. Cunningham et al. 2015) and H (L. Roth et al. 2017a). Callisto’s atmosphere likely also possesses an H₂O component, which is produced via sublimation and sputtering of surface water ice, and can further contribute to the dissociated products, O and H, as well as OH; however, the abundance of Callisto’s water vapor is not well constrained (e.g., S. R. Carberry Mogan et al. 2022).

It is expected that Callisto’s ionosphere is produced via photo- and magnetospheric electron-impact ionization of these atmospheric components and is thus composed of species similar to those in the atmosphere: C-, O-, and/or H-bearing ions. However,

the presence of Callisto’s ionosphere has only been detected by Galileo observations of plasma waves (D. A. Gurnett et al. 1997, 2000) and radio occultations (A. J. Kliore et al. 2002), from which the necessary densities of ionospheric electrons were inferred. From these electron densities, neutral sources have been suggested (e.g., D. A. Gurnett et al. 1997, 2000; A. J. Kliore et al. 2002), but there is a gap in knowledge about the ions present in Callisto’s ionosphere.

The Particle Environment Package (PEP) on board the Jupiter Icy Moons Explorer (Juice) will provide the first in situ observations of the ions present in Callisto’s ionosphere. Specifically, the Neutral and Ion Mass Spectrometer (NIM) is designed to detect thermal ions with energies \lesssim 10 eV, while the Jovian Plasma Dynamics and Composition (JDC) instrument extends these measurements to ions in the energy range of \sim 1 eV to \sim 40 keV (A. Galli et al. 2022). Prior to this work, only a limited number of studies have modeled the ionospheric composition at Callisto (e.g., M.-C. Liang et al. 2005; L. Liuzzo et al. 2015, 2016; O. Hartkorn et al. 2017). Therefore, in preparation for the eventual 20+ Juice flybys of Callisto in the 2030s (A. Galli et al. 2022), we address this knowledge gap here by applying a photochemical model to Callisto’s ionosphere produced via photo- and magnetospheric electron-impact ionization of its atmosphere, which is simulated by a molecular kinetics model, as well as the concomitant ion–neutral chemistry, while also taking into account diffusion and magnetospheric pickup of the nascent ions.

The remainder of this article proceeds as follows. In Section 2, we describe the in situ and remote observations of Callisto’s atmosphere and ionosphere (Section 2.1), as well as

³ Corresponding author.

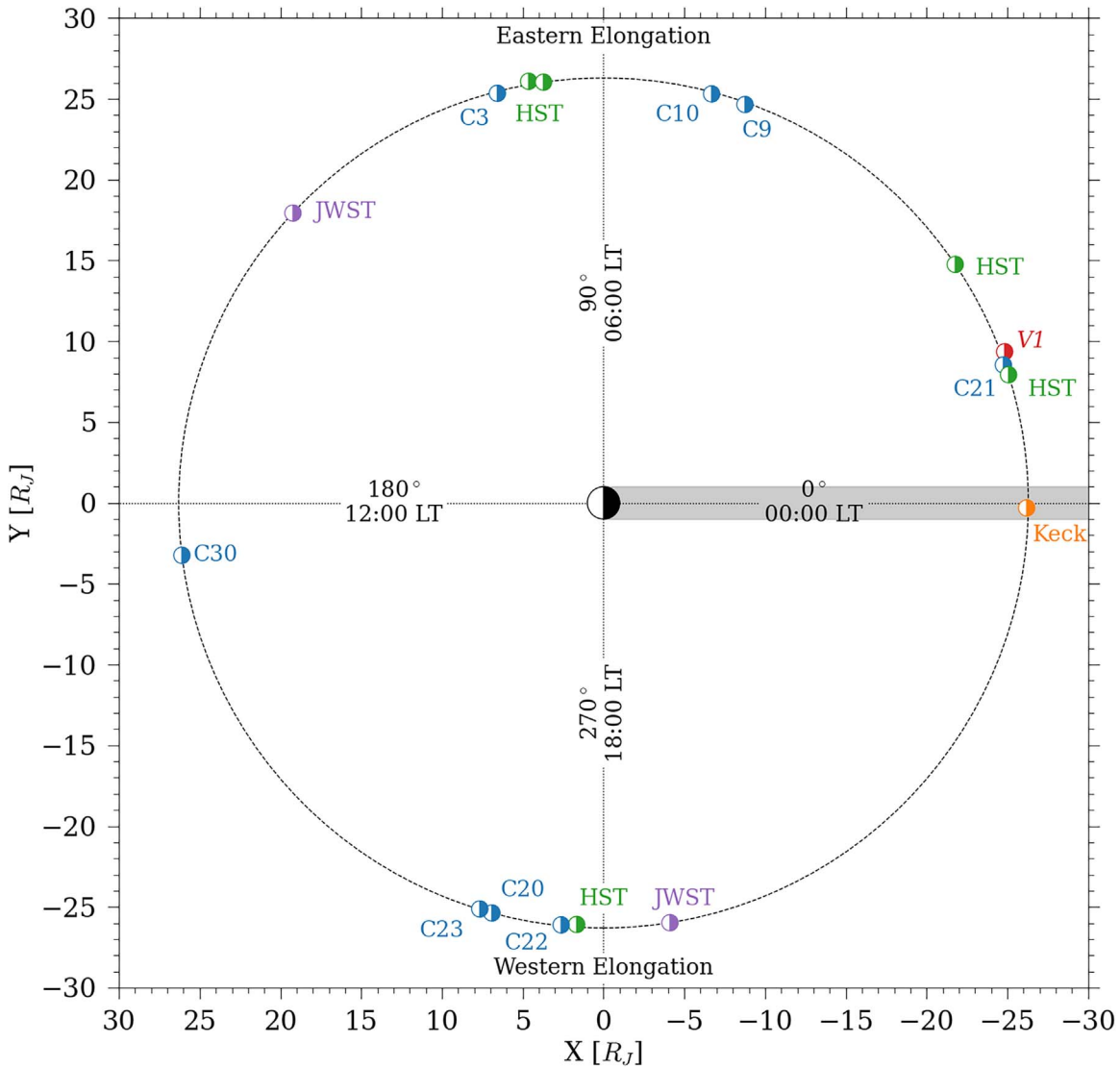


Figure 1. Orbital configuration of Callisto during the various observations described in Section 2.1, shown in units of Jupiter radii, $R_J = 71,492$ km: Voyager 1, “V1,” during its C/A to the Jovian system (A. L. Broadfoot et al. 1979; red); Galileo C3, C9, C10, C21–23, and C30 flybys (D. A. Gurnett et al. 1997, 2000; R. W. Carlson 1999; A. J. Kliore et al. 2002; blue); HST (D. F. Strobel et al. 2002; N. J. Cunningham et al. 2015; green); Keck (K. de Kleer et al. 2023; orange); and JWST (R. J. Cartwright et al. 2024; purple). The $+X$ -direction points toward the Sun, while the Y -axis lies in the ecliptic plane, aligned with Callisto’s counterclockwise orbital motion around Jupiter. Orbital longitude and local time as well as eastern and western elongations are also listed for reference.

the complementary modeling efforts motivating this study (Section 2.2). In Section 3, we describe the models used to simulate Callisto’s atmosphere (Section 3.1) and ionosphere (Section 3.2). Finally, in Section 4, we present the results of our models; in Section 5, we discuss the implications of these findings, in particular how they compare with previous observations and models at Callisto, as well as the recent Juno flybys of Europa and Ganymede, and how they can be used to guide future observations; and in Section 6, we conclude this study.

2. Background: Previous Observations and Models of Callisto’s Atmosphere and Ionosphere

2.1. Observations

Figure 1 illustrates the orbital configurations of Callisto during the observations described below.

Voyager 1 attempted to observe airglow emissions emanating from Callisto’s neutral atmosphere resulting from interactions with

solar photons or magnetospheric electrons as the spacecraft made its closest approach (C/A) to the moon (A. L. Broadfoot et al. 1979). However, the onboard ultraviolet (UV) spectrometer did not detect such emissions; only an upper limit of $5 \times 10^6 \text{ cm}^{-3}$ was calculated for O, and, due to uncertainties in the contribution of the background signal, no such constraint was made for H.

During Galileo’s first flyby of Callisto (C3), which had a C/A altitude of 1129 km, the spacecraft passed directly through the wake downstream of the corotating magnetospheric plasma as the sunlit and ram-side hemispheres were nearly opposite one another: when Callisto was near eastern elongation (i.e., an orbital longitude of 90° or local time of 06:00 LT). Galileo’s plasma-wave instrument (PWS) detected plasma oscillations at the upper hybrid frequency, from which electron densities ranging from ~ 5 to 100 cm^{-3} were inferred (D. A. Gurnett et al. 1997). These calculated densities were much larger than would be expected in the Jovian magnetosphere at Callisto’s orbit ($< 1 \text{ cm}^{-3}$), indicating that Callisto is the source of locally generated plasma; i.e., it possesses an ionosphere. Thus,

D. A. Gurnett et al. (1997) suggested that a neutral atmosphere must be present around Callisto in order to produce this plasma.

Only two other Galileo flybys recorded in situ plasma-wave signals suitable for determining electron densities: C10 and C22, for which the C/A altitudes were 535 km and 2299 km, respectively. Although in both trajectories, Galileo passed almost directly through the center of the geometric wake of the magnetospheric plasma, C10 occurred when Callisto was near eastern elongation, whereas C22 occurred when the sunlit and ram-side hemispheres aligned with one another: when Callisto was near western elongation (i.e., an orbital longitude of 270° or local time of 18:00 LT). Upper hybrid waves detected during the C10 flyby showed that Galileo passed through a dense plasma in the immediate vicinity of Callisto with peak electron densities of $\sim 400 \text{ cm}^{-3}$ (D. A. Gurnett et al. 2000), reaffirming the assessment of the C3 flyby that Callisto is a significant source of plasma (D. A. Gurnett et al. 1997). However, in contrast to C3 and C10, no evidence of enhanced electron densities in the downstream wake region was observed during the C22 flyby (D. A. Gurnett et al. 2000). Since enhanced electron densities were observed in the vicinity of but not far downstream of Callisto, D. A. Gurnett et al. (2000) suggested that this density distribution is characteristic of an ionosphere. Moreover, since large ionospheric densities were detected over the dayside during the C3 and C10 flybys and a much lower density was detected over the nightside during the C22 flyby, the authors suggested that solar illumination is a key contributor to its production.

Also during the C10 flyby, Galileo's near-infrared (IR) mapping spectrometer scanned the equatorial noon region from the surface to an altitude of ~ 300 km and detected a CO₂ atmosphere via airglow emissions (R. W. Carlson 1999). The spectral profile of the emission features was shown to be consistent with an isothermal CO₂ atmosphere with a temperature of 150 ± 50 K and surface density $n_{0,\text{CO}_2} \sim 4 \times 10^8 \text{ cm}^{-3}$, corresponding to a vertical column density of $\sim 8 \times 10^{14} \text{ cm}^{-2}$. Several possible atmospheric sources were suggested, such as radiolysis (R. E. Johnson 1990), in which CO₂ is produced via chemical reactions involving endo- or exogenic C-bearing surface materials. R. W. Carlson (1999) also speculated that dissociated products of CO₂ (e.g., CO, O) could be present in the atmosphere.

Radio occultation measurements were made by Galileo during six flybys of Callisto (C3, C9, C20, C22, C23, and C30; A. J. Kliore et al. 2002) with two occultations per flyby, as the spacecraft entered and exited the terminator regions. The first (C3) and last (C30) of these flybys were unable to produce any useful information using this technique, but the four intervening flybys (C9, C20, C22, and C23) were able to produce data relevant to Callisto's ionosphere. The first of these successful flybys (C9) occurred upstream of the magnetospheric plasma when Callisto was near eastern elongation, whereas the next three (C20, C22, and C23) occurred in the geometric wake when Callisto was near western elongation. During the C9 flyby, Galileo was unable to detect the presence of an ionosphere entering or exiting the terminator regions. The presence of an ionosphere was detected during the C20 ingress and egress, where peak electron densities of $\sim (4\text{--}5) \times 10^3 \text{ cm}^{-3}$ were derived $\sim 42\text{--}72$ km above the surface. Similar peak electron densities ($\sim (3\text{--}8.5) \times 10^3 \text{ cm}^{-3}$) were derived above the surface ($\sim 8\text{--}32$ km) during the egress of the C22 and C23 flybys. During the ingress of these flybys, however, even larger peak

electron densities, $\sim (1.5\text{--}1.7) \times 10^4 \text{ cm}^{-3}$, were derived at altitudes of $\sim 27\text{--}48$ km.

A. J. Kliore et al. (2002) was only able to infer information about the neutral atmosphere sourcing the “strong” detections (C22 and C23 ingress), i.e., those with peak electron densities ($> 10^4 \text{ cm}^{-3}$) that significantly exceed any error bars. From these strong detections, the necessary neutral densities were calculated assuming the atmosphere and ionosphere were composed of O₂ and O₂⁺, respectively; were spherically symmetric; and were in photochemical equilibrium (PCE)—i.e., O₂⁺ production (photo- and/or electron-impact ionization of O₂) is balanced by loss (dissociative recombination, DR), allowing for the continuity equation to be rearranged so that the corresponding O₂ density can be calculated. A. J. Kliore et al. (2002) estimated n_{0,O_2} in the range of $\sim (1\text{--}3) \times 10^{10} \text{ cm}^{-3}$, which, assuming O₂ scale heights of $\sim 15\text{--}24$ km, corresponded to column densities in the range of $\sim (3\text{--}4) \times 10^{16} \text{ cm}^{-2}$, ~ 2 orders of magnitude denser than those of the observed CO₂ component of the atmosphere (R. W. Carlson 1999).

Since an ionosphere was not detected via radio occultations when Callisto was near eastern elongation (C9) but only near western elongation (C20, C22, and C23), A. J. Kliore et al. (2002) suggested that the latter orbital configuration is required for an ionosphere to be produced via photo- and magnetospheric electron-impact ionization. However, this interpretation is contrary to the detections made by PWS: when Callisto was near eastern elongation during the C3 and C10 flybys, PWS detected plasma at significant distances from its surface (D. A. Gurnett et al. 1997, 2000), while a near-surface ionosphere was not detected via radio occultations during the C9 flyby (A. J. Kliore et al. 2002). Moreover, when Callisto was near western elongation during the C22 flyby, one of the largest near-surface electron densities was derived via radio occultations (A. J. Kliore et al. 2002), but PWS did not detect an enhanced plasma (D. A. Gurnett et al. 2000).

The Hubble Space Telescope (HST) Space Telescope Imaging Spectrograph (STIS) observed Callisto near eastern and western elongation, searching for UV emission features indicative of magnetospheric electron-impact excitation of CO₂, CO, and/or O₂ in its atmosphere, but was ultimately unable to detect their presence (D. F. Strobel et al. 2002). As a result, only upper limits for these species were calculated: 10^{17} cm^{-2} , $3 \times 10^{17} \text{ cm}^{-2}$, and 10^{18} cm^{-2} for CO, O₂, and CO₂, respectively, with the values for O₂ and CO₂ being in excess of those suggested from Galileo observations (R. W. Carlson 1999; A. J. Kliore et al. 2002). Upper limits were also calculated for C (10^{13} cm^{-2}) and O ($2.5 \times 10^{13} \text{ cm}^{-2}$). D. F. Strobel et al. (2002) attributed these nondetections to the Jovian magnetospheric thermal plasma being largely diverted around Callisto due to the relatively low strength of the Jovian magnetic field at its orbit and the large conductances of its ionosphere. As a result, penetration of magnetospheric electrons into Callisto's atmosphere would be severely inhibited and thus could not be the source of its observed near-surface ionosphere observed during Galileo radio occultations (A. J. Kliore et al. 2002), instead implying that solar illumination must be the dominant source, consistent with earlier interpretations of Galileo PWS observations (D. A. Gurnett et al. 1997, 2000).

More than a decade after the initial HST/STIS observations were made, UV emissions produced by O were detected by HST using its newly installed Cosmic Origins Spectrograph (COS)

when Callisto was near eastern elongation (N. J. Cunningham et al. 2015). N. J. Cunningham et al. (2015) determined that the CO₂ atmosphere detected by R. W. Carlson (1999) was too thin to produce detectable UV emissions from photo- or electron-impact dissociative excitation. Instead, the authors suggested that the measured brightness of the emissions implied that dissociative excitation of O₂ was the parent source, rather than that of H₂O or direct excitation of O. Furthermore, they suggested that impacts by photoelectrons rather than magnetosphere electrons were the source of the excitation. Thus, they concluded that the detected UV emissions are generated by photoelectrons produced via the ionization of an O₂-dominated atmosphere with a column density of $\sim 4 \times 10^{15} \text{ cm}^{-2}$, which is about an order of magnitude less than that calculated by A. J. Kliore et al. (2002) when Callisto was near western elongation.

L. Roth et al. (2017a) revisited the HST/STIS observations made by D. F. Strobel et al. (2002) in search of extended emissions from a H corona. Faint atmospheric emissions were successfully detected above the limb of Callisto originating from resonant scattering of solar photons by H. L. Roth et al. (2017a) suggested dissociation of water vapor is likely the primary source of H near the subsolar point, where the surface temperatures and hence sublimation rates are the highest, while beyond this region, a global, radiolytically produced H₂ component could be the dominant source.

Optical auroral emissions emanating from Callisto's atmosphere were detected with the Keck telescope while the moon was in eclipse, which was interpreted as originating from an O₂ component (K. de Kleer et al. 2023). Unlike in the HST/COS observation (N. J. Cunningham et al. 2015), photoelectrons could not be the source of the emissions since Callisto was shielded from solar photons by the disk of Jupiter. Therefore, K. de Kleer et al. (2023) suggested that magnetospheric electron impacts were responsible for producing the emissions. Despite the differences in suggested sources—photo- versus magnetospheric electron impacts—both N. J. Cunningham et al. (2015) and K. de Kleer et al. (2023) arrived at roughly the same disk-averaged O₂ column density required to produce the independently detected emissions: $\sim 4 \times 10^{15} \text{ cm}^{-2}$.

The James Webb Space Telescope (JWST) near-IR spectrograph (NIRSpec) detected CO₂ rovibrational emission lines over Callisto's leading and trailing hemispheres (R. J. Cartwright et al. 2024) indicative of a CO₂ atmosphere. Whereas CO₂ was first observed by Galileo over the leading hemisphere, these JWST/NIRSpec observations represent the first detection of CO₂ over the trailing hemisphere, affirming the presence of a global CO₂ component in Callisto's atmosphere. Column densities in the range of $\sim (0.4\text{--}1) \times 10^{15} \text{ cm}^{-2}$ were inferred by R. J. Cartwright et al. (2024) over both hemispheres, consistent with that inferred from the Galileo observation (R. W. Carlson 1999).

2.2. Models

M.-C. Liang et al. (2005) applied a 1D photochemical model to Callisto's atmosphere and ionosphere to reproduce the electron densities detected by A. J. Kliore et al. (2002) while satisfying the upper limits constrained by D. F. Strobel et al. (2002). The model of M.-C. Liang et al. (2005) simulated several chemical reactions between neutral and ionized species assuming the atmosphere was isothermal up to an altitude of 350 km above Callisto's surface at a solar zenith angle (SZA) of 80°, which is similar to those during the ingress of the C22 (78.7°) and C23 (82.5°) flybys. Consistent with A. J. Kliore et al.

(2002), they suggested that an O₂ atmosphere $n_0 \sim 2$ orders of magnitude larger than that inferred for CO₂ (R. W. Carlson 1999) is required to produce the electron densities detected during Galileo radio occultations. M.-C. Liang et al. (2005) considered two models of Callisto's atmosphere: with and without sublimated water vapor. In the former case, the column density of O exceeded the upper limit set by D. F. Strobel et al. (2002), while in the latter case, OH radicals produced by photo- and electron-impact dissociation of H₂O removed O atoms via the reaction O + OH → O₂ + H to reduce the O column density below this threshold.

O. Hartkorn et al. (2017) generated a 3D model of Callisto's ionospheric electron population according to a prescribed atmosphere composed of H₂O, CO₂, and O₂. Whereas the CO₂ component was assumed to be spherically symmetric, the H₂O and O₂ components were assumed to have a day/night asymmetry. Ionization by EUV photons and photoelectrons was considered as the source for ionospheric electrons, while UV emissions were only generated by the latter. Based on these constraints, they explained the ionospheric observations made by A. J. Kliore et al. (2002) and the UV emissions observed by N. J. Cunningham et al. (2015). They suggested that the electron densities were especially sensitive to the presence of H₂O: the larger the H₂O abundance, the more electron cooling occurred via rotational state excitation of H₂O (e.g., Y. Itikawa & N. Mason 2005), leading to increased DR and, as a result, lower electron densities. In agreement with Galileo plasma-wave observations (D. A. Gurnett et al. 2000), they also demonstrated that an ionosphere can form when Callisto is at eastern elongation, conflicting with the suggestion made by A. J. Kliore et al. (2002) that an ionosphere can only form when the moon is at western elongation.

S. R. Carberry Mogan et al. (2022) implemented a molecular kinetics model to constrain the sources of Callisto's H corona detected by HST/STIS (L. Roth et al. 2017a). Assuming the atmosphere was composed of sublimated H₂O, radiolytically produced O₂ and H₂, and the hot H produced via photo- and magnetospheric electron-impact dissociation of H₂O and H₂, they demonstrated that dissociation of H₂O cannot explain the observed morphology of the H corona, while dissociation of a global H₂ component can, thereby providing the first evidence of H₂ in Callisto's atmosphere. Furthermore, they demonstrated that above certain densities, the sublimated H₂O absorbed Lyα emitted from the surface, while the Lyα emitted by its dissociated product H produced a peak in emissions on Callisto's disk brighter than that observed by HST (e.g., see Figures 8–10 in S. R. Carberry Mogan et al. 2022). Thus, in order for the sublimated H₂O to not produce emissions inconsistent with those observed by HST/STIS, they placed upper limits on the H₂O sublimation flux ($\lesssim 10^{12} \text{ cm}^{-2} \text{ s}^{-1}$) and the corresponding number density ($\lesssim 10^8 \text{ cm}^{-3}$) and column density ($\lesssim 10^{15} \text{ cm}^{-2}$). These upper limits are 1–2 orders of magnitude less than those implemented by M.-C. Liang et al. (2005) and O. Hartkorn et al. (2017).

R. Yasuda et al. (2024) recently applied a ray-tracing model to simulate Galileo radio occultations of Callisto's ionosphere during the C9 and C30 flybys, for which they calculated peak electron densities of 350 cm^{-3} and 12.5 cm^{-3} , respectively. These occultations occurred over the nightside of Callisto, and their derived electron densities were well below even the lowest peaks observed during the C20, C22, and C23 occultations, which occurred over the dayside (A. J. Kliore et al. 2002). Thus,

they suggested that Callisto's ionosphere on the dayside is dominated by the ionization of sublimated H₂O, which peaks above the subsolar point, implying that the ionized H₂O⁺ and the accompanying electrons would not significantly contribute to the electrons observed on the nightside of the terminator regions. They suggest that this is consistent with the model of A. Vorburger et al. (2015), who simulated sublimation of H₂O according to a warm subsolar surface temperature of 165 K. However, R. Yasuda et al. (2024) did not consider two key findings: (1) S. R. Carberry Mogan et al. (2022) showed that the estimates made by A. Vorburger et al. (2015) for sublimation flux and the resultant H₂O densities are at least ~ 2 orders of magnitude too large, and (2) Callisto's O₂ (N. J. Cunningham et al. 2015; K. de Kleer et al. 2023) and CO₂ (R. W. Carlson 1999; R. J. Cartwright et al. 2024) components are denser than H₂O and are globally distributed throughout the atmosphere. Therefore, ionization of global O₂ and CO₂ should result in at least a quasi-global ionosphere, which is sourced on the dayside by solar illumination and magnetospheric electron impacts and on the nightside only by the latter. Moreover, the study by R. Yasuda et al. (2024) did not consider the role that magnetospheric pickup of the nascent ions would play in distributing the ionospheric population around Callisto. Studies of this interaction between Callisto's ionosphere and its magnetospheric environment have shown that these ions suffuse throughout Callisto's local environment, traveling far from their generation region (e.g., L. Liuzzo et al. 2015, 2016). In addition, C. M. Haynes et al. (2023) recently applied a hybrid plasma model to Europa's environment, demonstrating that, even though ionization of sublimated H₂O peaks near the subsolar point, the gyroradii of these picked-up ionospheric particles are comparable to the size of the moon, generating significant H₂O⁺ densities near its terminators (see Figure 4 therein). Although the dynamics of picked-up H₂O⁺ ions have not yet been investigated at Callisto, the local Jovian magnetic field is up to 2 orders of magnitude weaker there than it is at Europa (M. G. Kivelson et al. 2004), resulting in even larger H₂O⁺ gyroradii and potentially allowing for a substantial population of H₂O⁺ to reach Callisto's terminators, where these radio occultations occur. Hence, while the ray-tracing models of R. Yasuda et al. (2024) provide an interesting technique to interpret future spacecraft observations, such as those made by Juice, their application to Galileo radio occultations and their interpretations of Callisto's atmosphere and ionosphere need to be reevaluated.

3. Method

In Sections 3.1 and 3.2, we describe the numerical models implemented here to simulate Callisto's atmosphere and ionosphere, respectively.

3.1. Atmosphere Model

At the densities inferred from observations (R. W. Carlson 1999; A. J. Kliore et al. 2002; N. J. Cunningham et al. 2015; S. R. Carberry Mogan et al. 2022; K. de Kleer et al. 2023; R. J. Cartwright et al. 2024), Callisto's atmosphere is collisional, necessitating a molecular kinetics model to accurately capture the influence of collisions therein. Indeed, previous studies by S. R. Carberry Mogan et al. (2020, 2021a, 2021b, 2022) have employed the direct simulation Monte Carlo (DSMC) method (G. A. Bird 1994)

to demonstrate that collisions significantly affect fundamental processes in Callisto's atmosphere, including thermal and nonthermal escape and day-to-night transport, as well as the interpretation of observational data. The DSMC method simulates macroscopic gas dynamics via stochastic microscopic processes using computational particles, each representing many real atoms or molecules. Here we implement the DSMC method to simulate radiolytically produced CO₂, H₂, and O₂, as well as the CO, H, and O produced via photo- and magnetospheric electron-impact dissociation of their parent molecules in Callisto's atmosphere. A 1D spherically symmetric simulation domain is employed in which radial cells are generated from Callisto's surface, $r_0 = R_C = 2410.8$ km, to its Hill sphere, $r_{HS} = (M_C/(3 M_J))^{1/3} d_{JC} \sim 20.8 R_C$. Here $M_C = 1.08 \times 10^{23}$ kg and $M_J = 1.898 \times 10^{27}$ kg are the masses of Callisto and Jupiter, respectively, and $d_{JC} \sim 26.3 R_J$ is the distance between Jupiter and Callisto in Jovian radii, $R_J = 71,492$ km. If a particle's trajectory crosses r_0 or r_{HS} , it is removed from the simulation. This network of cells allows for particles to be locally grouped based on their position to simulate collisions as well as to calculate average macroscopic properties of the atmosphere, such as local densities and temperatures. The simulations presented herein were run for a sufficiently long duration (e.g., see S. R. Carberry Mogan et al. 2021b) such that these physical parameters reach a steady state.

Here we treat the CO₂, H₂, and O₂ components as in our earlier models of Callisto's atmosphere: they are assumed to be in a steady state, thermally desorbing from the surface with a flux, Φ , calculated as a function of a prescribed surface density, n_0 , and temperature, T_0 : $\Phi_i = (n_0 v_i(T_0))/4$. Here, the species i represents either CO₂, H₂, or O₂; $v_i(T_0) = \sqrt{8k_B T_0 / (\pi m_i)}$ is the mean Maxwellian speed, where k_B is the Boltzmann constant and m_i is the molecular mass; and we set $T_0 = 167$ K and 80 K, which approximately correspond to Callisto's subsolar (SZA = 0°) and terminator (SZA = 90°) surface temperatures (e.g., S. R. Carberry Mogan et al. 2022, Figure 1 therein), respectively. For H₂, we set $n_{0,H_2} = 4 \times 10^7$ cm⁻³, which S. R. Carberry Mogan et al. (2022) showed is capable of reproducing the H corona detected by HST (L. Roth et al. 2017a). For O₂, we set $n_{0,O_2} = 10^9$ cm⁻³, which S. R. Carberry Mogan et al. (2022) reproduced the disk-average column densities suggested by N. J. Cunningham et al. (2015). For CO₂, we set $n_{0,CO_2} = 4 \times 10^8$ cm⁻³, the value inferred by R. W. Carlson (1999) to reproduce the airglow emissions detected by Galileo, which results in a column density consistent with the more recent JWST observations (R. J. Cartwright et al. 2024). For convenience, Table 1 lists the physical parameters implemented at r_0 in the DSMC simulations presented herein. Note that the prescribed values for $n_{0,i}$ determine a fixed Φ_i , but the simulated number densities at the surface (i.e., in the lowermost radial cell) can differ slightly as particles are constantly releasing from and returning to the surface as well as being lost via interactions with solar photons and magnetospheric electrons.

CO₂, H₂, and O₂ particles are injected into the simulation domain uniformly across Callisto's surface using a cosine distribution with respect to the surface normal with velocities sampled from a T_0 -dependent Maxwellian flux distribution (e.g., R. T. Brinkmann 1970; G. R. Smith et al. 1978). While particles moving solely under gravitational acceleration would follow Keplerian orbits, in our DSMC simulations, their trajectories are perturbed by binary collisions. To capture both

Table 1

Model Inputs Implemented at Callisto's Surface, $r_0 = R_C = 2410.8 \text{ km}$	
Physical Parameter (Units)	Value
Solar zenith angle (deg)	0 90
Temperature, T_0 (K)	167 80
Number density, n_0 ($\times 10^8$) cm^{-3}	O ₂ 10 CO ₂ 4.0 H ₂ 0.4

the continuous gravitational acceleration and the abrupt velocity changes from collisions, we track their motion by solving a fourth-order Runge–Kutta integration at each time step. Elastic collisions between these molecules are simulated using the variable hard sphere (VHS) model (G. A. Bird 1994) to determine the relative speed-dependent collision cross section, assuming the particles scatter isotropically.

Interactions with photons and magnetospheric electrons dissociate and/or ionize these molecules. Whereas a particle representing an atom or molecule is removed from the simulation when ionized, if a particle representing a molecule is dissociated, it leads to the nonthermal production of CO, O (from O₂ and CO₂), or H. We refer the reader to S. R. Carberry Mogan et al. (2022) for a discussion of how these reactions are implemented in a DSMC simulation (Section 2.3.2 therein). The additional neutral species produced via photochemistry are not considered in this study but are the subject of future work. Given the implemented lower boundary condition, the CO component in our simulation is relatively thin. Consequently, any C and O produced via dissociation of CO would be even less significant; therefore, we do not track these dissociated products as particles. As discussed in Section 5.4, we defer an exploration of the evolution of Callisto's CO—including factors such as nonunity sticking coefficients, a more likely representation of the highly volatile species—and its dissociated products to future work. Elastic collisions between dissociated CO and the other molecules are simulated using the VHS model, and the particles are assumed to scatter isotropically. Elastic collisions between atoms (O and H) and molecules (H₂, O₂, CO, and CO₂) are simulated using the model of N. R. Lewkow & V. Kharchenko (2014) to determine collision cross sections and scattering angles, both of which are a function of the corresponding differential cross-section distribution.

3.1.1. Photolytic and Electron-impact Reaction Rates

Figure 2 compares the frequency of the photolytic reactions considered as a function of solar activity. These rates are taken from W. F. Huebner & J. Mukherjee (2015) for an “active” (solar maximum) and “quiet” (solar minimum) Sun, with solar median representing the average between these values, all of which are scaled to 5.2 au. In the DSMC and photochemical simulations presented herein, we assume solar median when determining photolytic reaction rates.

In Figure 2, these rates are compared to the analogous magnetospheric electron-impact rates assuming two upstream number densities and temperatures: $n_e = 0.1 \text{ cm}^{-3}$ and 1 cm^{-3} , $T_e = 40$ and 400 eV . These ranges of n_e and T_e are meant to represent the high variability and uncertainties in Callisto's local plasma environment, demonstrating the order-of-magnitude changes in physical parameters like density and

temperature (E. C. Sittler & D. F. Strobel 1987; F. M. Neubauer 1998; M. G. Kivelson et al. 2004; T. K. Kim et al. 2020). The electron-impact rates are calculated by convolving these n_e and T_e values assuming a Maxwellian distribution with the various electron-impact collision cross sections illustrated in Figures A1–A5 in Appendix A.

On the one hand, when $n_e = 0.1 \text{ cm}^{-3}$, regardless of T_e , all of the electron-impact reactions except ionization of H₂ occur less frequently than photolytic reactions at solar median. On the other hand, when $n_e = 1 \text{ cm}^{-3}$, all of the electron-impact reactions except dissociation of CO₂ and O₂ occur as frequently as or more than those induced by interactions with photons at solar median. Therefore, we only consider two cases involving magnetospheric electron-impact reactions in the presented DSMC and photochemical simulations, both with $n_e = 1 \text{ cm}^{-3}$ and one with $T_e = 40 \text{ eV}$ and the other with $T_e = 400 \text{ eV}$. At the lower temperature, dissociation tends to occur more frequently, whereas at the higher temperature, ionization occurs more frequently. This is a result of where the corresponding electron-impact cross sections peak (Figures A1–A5).

All of the electron-impact reaction rates listed in Figure 2 neglect energy deposition in Callisto's atmosphere. To take this into account, we first run a DSMC simulation that only considers interactions with photons leading to ionization and dissociation. Based on the resultant density profiles, we then determine the energy deposited by the flux of electrons at the top of the atmosphere en route to the surface in a model similar to that of (S. R. Carberry Mogan et al. 2023a), as illustrated in Figures B1 and B2 in Appendix B. As can be seen, consistent with S. R. Carberry Mogan et al. (2023a), the inverse energy dependence of electron-impact-stopping cross sections causes electrons with lower T_e to undergo more collisions and deposit greater energy in the atmosphere than those with higher T_e . We use the resultant density and temperature distributions to calculate the local electron-impact reaction rates implemented in the subsequent DSMC and photochemical models.

3.2. Ionosphere Model

The photochemical model that we used to simulate Callisto's atmosphere was originally developed for the ionospheres of the gas giants (e.g., L. E. Moore et al. 2004, 2019). This 1D spherically symmetric model solves the coupled set of ion continuity equations via explicit time integration to specify ion transport and chemical kinetics. Additional reactions appropriate for Callisto's ionosphere have been added to those given in L. E. Moore et al. (2018); see Tables C1–C19 in Appendix C for all of the reactions implemented in this model.

Ion production follows from photoionization by solar EUV photons. Absorption of solar photons via the Beer–Lambert law is treated within the model. Photoabsorption is negligible at $\text{SZA} = 0^\circ$, as the optical depth of EUV photons in Callisto's atmosphere is <1 . Therefore, photoionization frequencies appropriate for Callisto's distance from the Sun (e.g., Figure 2) should work as effectively for atmospheres comparable to Figure 3. However, near the terminator ($\text{SZA} \sim 90^\circ$), photoabsorption becomes nonnegligible and affects photolytic reaction rates close to the surface (e.g., M.-C. Liang et al. 2005). Simulations here are performed for solar median conditions corresponding to an F10.7 cm radio flux of $120 \times 10^{-22} \text{ W m}^{-2} \text{ Hz}^{-1}$, with the solar spectrum specified by extrapolating the daily EUV and soft X-ray fluxes measured

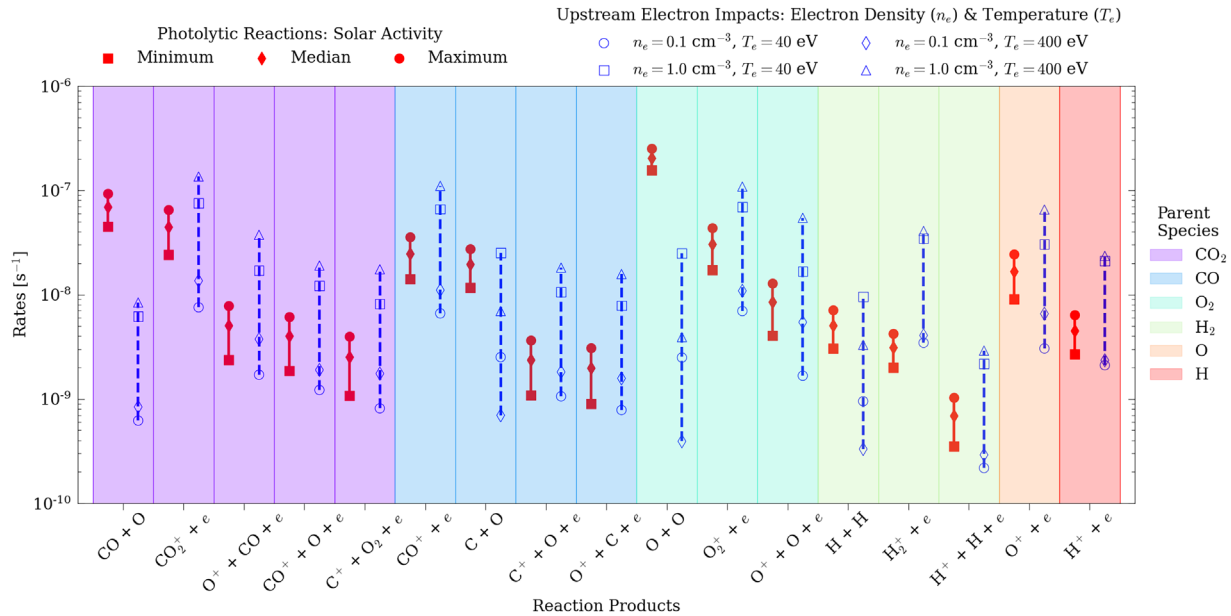


Figure 2. A comparison of dissociation and/or ionization rates resulting from interactions with photons and magnetospheric electrons in Callisto’s atmosphere composed of CO_2 (purple), CO (blue), O_2 (cyan), H_2 (light green), O (orange), and H (red). A range of photodissociation and/or ionization rates (solid red lines) are listed according to solar minimum (filled red squares), median (filled red diamonds), and maximum (filled red circles). A range of magnetospheric electron-impact dissociation and/or ionization rates (dashed blue lines) are listed assuming the following electron number densities, n_e , and temperature, T_e : $n_e = 0.1 \text{ cm}^{-3}$, $T_e = 40 \text{ eV}$ (open blue circle); $n_e = 1.0 \text{ cm}^{-3}$, $T_e = 40 \text{ eV}$ (open blue square); $n_e = 0.1 \text{ cm}^{-3}$, $T_e = 400 \text{ eV}$ (open blue diamond); and $n_e = 1.0 \text{ cm}^{-3}$, $T_e = 400 \text{ eV}$ (open blue triangle).

by the Thermosphere Ionosphere Mesosphere Energetics and Dynamics Solar EUV Experiment (T. N. Woods et al. 2005) to Callisto (e.g., L. E. Moore et al. 2018). While photoelectrons and their secondaries can lead to additional ionization, “secondary ionization” is not treated in this work, as it typically only overtakes primary ionization rates at relatively high optical depths (M. Galand et al. 2009), where the most energetic photons are absorbed in an atmosphere, and in this case those photons penetrate to Callisto’s surface. Instead, a much larger source of additional ionization follows from magnetospheric electron impacts (described in Section 3.1.1), which dominate photoionization rates when included.

Vertical ion transport follows from ambipolar diffusion with a $\sin^2 I$ correction by default, where I is the magnetic dip angle. For this study, we assume that the magnetic field within Callisto’s ionosphere is vertical, meaning vertical plasma motion in 1D is not reduced by the factor of $\sin^2 I$. Additional ion transport results from the local acceleration of ionospheric ions by electric fields that are generated by Callisto’s interaction with the Jovian magnetospheric plasma. Near Callisto’s surface, these electric fields are primarily formed from the electron pressure gradient and/or Hall terms as opposed to the convective term (e.g., L. Liuzzo et al. 2015), since the local plasma velocity drops to 0. For convenience, we refer to this ion acceleration generally as “ion pickup”; however, the reader should bear in mind that this includes the sum of the perpendicular convection, electron pressure gradient, and Hall acceleration terms. To implement this ion acceleration within the photochemical model, we extract ionospheric pickup velocities from the Adaptive Ion-Kinetic Electron-Fluid (AIKEF) modeling results of L. Liuzzo et al. (2022) and impose them for all ion species using a simple advection scheme in addition to the speed obtained from diffusion. To constrain the plasma interaction within Callisto’s local magnetospheric environment, L. Liuzzo et al. (2022) used

the AIKEF hybrid plasma model, which treats ions as particles and electrons as a massless, charge-neutralizing fluid; for further details on AIKEF, we refer the reader to L. Liuzzo et al. (2015, 2016, 2017, 2018, 2019a, 2019b, 2024), S. R. Carberry Mogan et al. (2023b), and C. M. Haynes et al. (2023, 2025). This interaction results in ion velocities that are negligible near Callisto’s surface but increase to $\sim 10 \text{ km s}^{-1}$ by $\sim 350 \text{ km}$ and reach $\sim 60 \text{ km s}^{-1}$ by $\sim 1000 \text{ km}$. Ionospheric pickup ion velocities were taken from a radial slice centered at the subram point of Callisto as representative of the average pickup ion velocity around the moon. While this is an approximation of the fully 3D variation in pickup ion speed around Callisto, it nevertheless suffices for investigating the impact on the 1D photochemical model. Future work with a higher-dimensional DSMC+photochemical model can be used to address more complex pickup ion motion.

In a steady state, the 1D ion continuity equation reduces to $v \frac{dn}{dr} + n \frac{dv}{dr} = S$, where v and n are ion velocities and number densities, respectively; r is the radial altitude; and S is the source term. Near the surface, the density gradient ($\frac{dn}{dr}$) of the ionosphere mirrors that of the atmosphere, as the ions are sourced from the neutrals and chemistry dominates over transport. However, at high altitudes, S becomes negligible, and $\frac{dn}{dr} \sim -(n/v) \frac{dv}{dr}$. Since the imposed ion pickup velocities quickly dominate those obtained from ambipolar diffusion and have a positive gradient ($\frac{dv}{dr} > 0$), $\frac{dn}{dr} \propto -v^{-1} \frac{dv}{dr}$ as ions are effectively siphoned upward from the source region until reaching the upper boundary, where a fixed velocity topside boundary condition is enforced.

Ionospheric ion and electron temperatures are set equal to the neutral temperature. While this is likely an unrealistic assumption, especially at high altitudes, where the influence of magnetospheric plasma dominates, it is a reasonable first step, as photochemistry will be seen to only dominate within

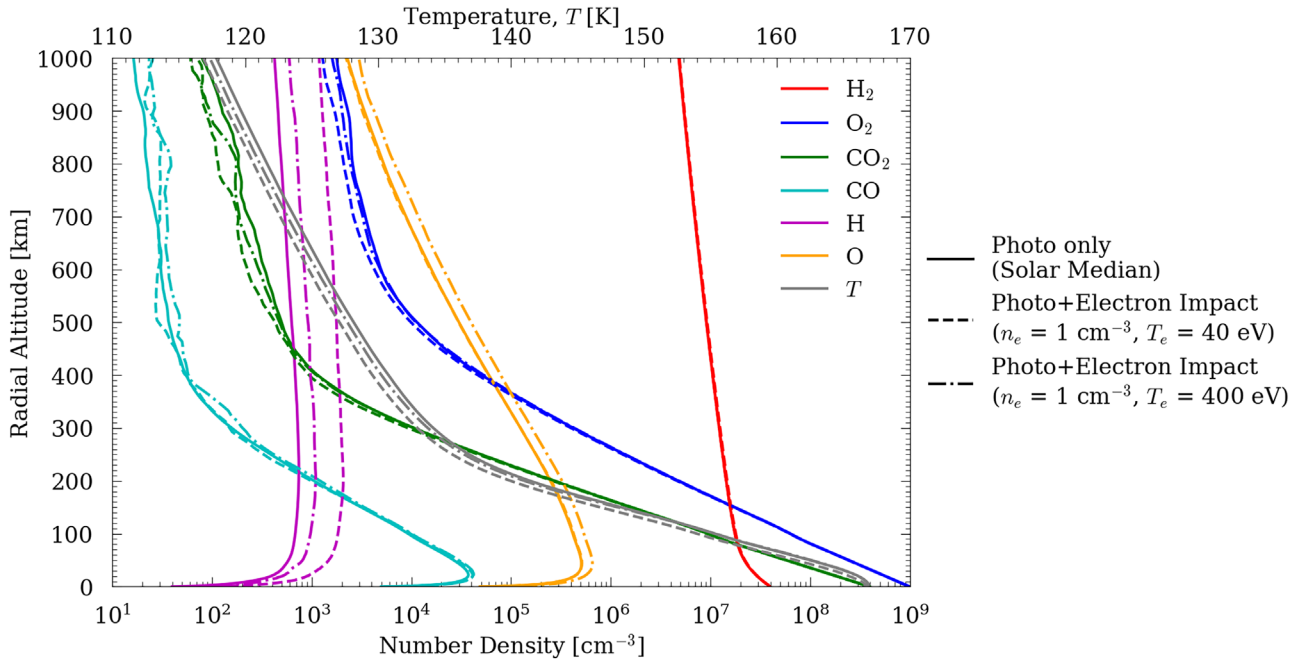


Figure 3. Results from DSMC models of Callisto’s atmosphere at $SZA = 0^\circ$ considering interactions with photons only (“Photo Only”; solid lines) compared to those considering interactions with photons and magnetospheric electrons (“Photo+Electron Impact”) assuming an upstream density, n_e , of 1 cm^{-3} and temperatures, T_e , of 40 eV (dashed lines) or 400 eV (dashed-dotted lines). Number densities (bottom x-axis) are listed as a function of radial altitude (y-axis) for H_2 (red), O_2 (blue), CO_2 (green), CO (cyan), H (magenta), and O (orange). The corresponding temperature profiles (top x-axis) are also illustrated in gray.

the first ~ 10 km above Callisto’s surface (Section 4.2.2). For otherwise identical conditions, the ion densities presented here thus represent a lower limit, as increasing T_e results in slower chemical loss rates. For example, if T_e were 10^4 K rather than ~ 100 K, in PCE, the recombination rate of O_2^+ would be a factor of ~ 25 slower and the resulting O_2^+ densities 5× larger.

4. Results

4.1. Callisto’s Atmosphere

Figure 3 illustrates the neutral density and temperature profiles from the three DSMC simulations carried out at $SZA = 0^\circ$: (1) only interactions with photons were considered (solid lines), and interactions with photons *and* magnetospheric electrons were considered, where at the top of the atmosphere the latter was assumed to have a density of $n_e = 1 \text{ cm}^{-3}$ and a temperature of either (2) $T_e = 40$ eV (dashed lines) or (3) $T_e = 400$ eV (dashed-dotted lines). Our results suggest that all of the species considered should be detectable above the C/A altitudes of the Juice encounters (on the order of 200 km) according to the PEP/NIM detection threshold of $\sim 1 \text{ cm}^{-3}$ (A. Galli et al. 2022).

The neutral density profiles of the major components of Callisto’s atmosphere (O_2 , CO_2 , and H_2) are largely unaffected by the inclusion of electrons in the DSMC simulations. Their density profiles are essentially the same up to ~ 500 km with or without including electrons, and above that there are only slight differences, which could be attributed to statistical noise given the relatively low particle count. Above ~ 400 – 500 km, the nonthermal tails of O_2 and CO_2 produced by collisions with the dissociated products, primarily the hot O produced via dissociation of O_2 (e.g., S. R. Carberry Mogan et al. 2024), become pronounced by the abrupt increase in their scale height. For H_2 , there is effectively no difference that can be discerned

up to at least 1000 km, because, unlike O_2 and CO_2 , the species is inherently highly extended and can escape without nonthermal collisions. Additionally, consistent with S. R. Carberry Mogan et al. (2022), for $n_{0,\text{H}_2} \sim 4 \times 10^7 \text{ cm}^{-3}$ at $SZA = 0^\circ$, the H_2 component remains collisional above the altitude range illustrated in Figure 3, with an exobase at ~ 1800 km. Since ion–neutral and ion–ion collision cross sections are larger than those for neutral–neutral ones due to long-range Coulomb interactions in collisions involving ions, the *plasma exobase* is generally located at higher altitudes than the neutral exobase (R. Schunk & A. Nagy 2009). Consequently, throughout the entire simulated altitude range of the photochemical model, both the atmosphere and the ionosphere remain collisional.

In contrast to the density profiles of their parent species, much larger differences are discernible in those of H and O when magnetospheric electron impacts are included. When $n_e = 1 \text{ cm}^{-3}$ and $T_e = 40$ eV, electron-impact dissociation of H_2 becomes the dominant source of H (see Figure 2), and as a result, the H density profile is the most dense in this case. Although electrons with $T_e = 400$ eV are far less efficient at dissociating H_2 than 40 eV electrons, they still contribute to the total H population, resulting in more H when these electrons are considered in addition to photodissociation of H_2 . However, the opposite trend is true for the O produced, where photodissociation of O_2 and CO_2 are the dominant sources of O , regardless of the considered n_e and T_e . However, at $T_e = 400$ eV, electron-impact dissociative ionization of O_2 producing neutral O (and ionized O^+) is more efficient than with $T_e = 40$ eV, and as a result, a slightly denser O population at the former T_e is produced. Since photodissociation of CO_2 is by far the dominant source of CO , there are only minor contributions to CO from electron-impact dissociative ionization, which only become pronounced at higher altitudes;

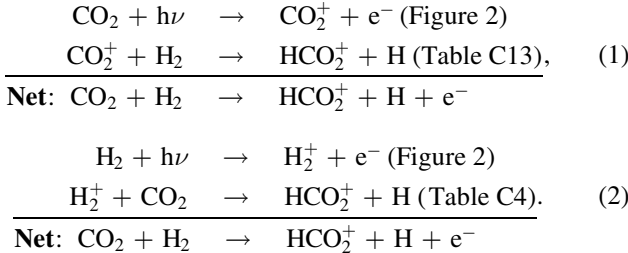
however, these results are also noisy given the relatively low particle count.

The temperature profiles in these DSMC simulations illustrated in Figure 3 are weighted averages among the considered species. Since there are only subtle differences in the simulated density profiles, the temperature profiles only differ slightly from each other. These differences in temperature are mostly a result of the slightly different escape rates; e.g., the most escape occurs with $n_e = 1 \text{ cm}^{-3}$ and $T_e = 40 \text{ eV}$, and as a result, the temperature profile cools the most. Interestingly, all of the simulated species were able to escape as a result of nonthermal collisions in the atmosphere. Although the temperature decreases with altitude as expected (S. R. Carberry Mogan et al. 2020), at $\sim 300 \text{ km}$, there is a sharp transition in the atmospheric scale height: from the surface to the altitude where this transition occurs, the temperature drops $\sim 30 \text{ K}$, but from there to $\sim 1000 \text{ km}$, the temperature only drops by about $\sim 15 \text{ K}$.

4.2. Callisto's Ionosphere

Figure 4 illustrates the ion density profiles from the photochemical model in which only interactions with photons were considered as external ionization sources. We only show results up to 1000 km as the ionospheric ions will undergo more complex 3D pickup at greater altitudes as they leave Callisto's vicinity. Such dynamics cannot be captured in the 1D photochemical model used here and are left for future work. We compare these results to the Juice/PEP/NIM density and energy thresholds of $\sim 1 \text{ cm}^{-3}$ and $\sim 10 \text{ eV}$, respectively, above the spacecraft's C/A altitude of $\sim 200 \text{ km}$ (A. Galli et al. 2022); above this energy threshold, ions can only be detected by Juice/PEP/JDC depending on measured differential fluxes and the instrument's integration time.

As expected, given the neutral inputs (Figure 3), O_2^+ is the dominant ion in Callisto's ionosphere. A surprising result, however, is the second-most (albeit more than an order of magnitude less than the most) dominant ion: HCO_2^+ . This ion is produced via several ion-neutral chemical reaction pathways; e.g.,

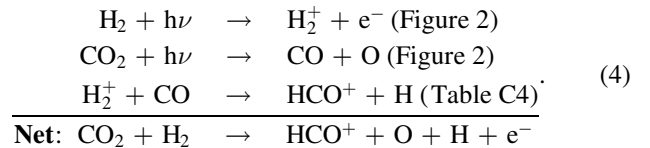
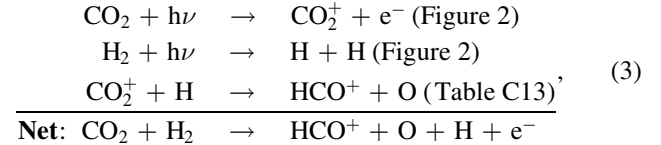


However, since HCO_2^+ is the heaviest ion in Callisto's ionosphere, its energy ($\frac{1}{2}mv^2$, where m and v are the ion's mass and speed, respectively), which is driven largely by magnetospheric pickup, quickly reaches the upper limit of NIM (A. Galli et al. 2022). Thus, although the HCO_2^+ density is above the NIM density limit up to at least 1000 km, it is only detectable by JDC above $\sim 290 \text{ km}$, where its energy exceeds the NIM upper limit.

Below $\sim 100 \text{ km}$, CO_2^+ is the third-densest species, produced via direct ionization of CO_2 . From ~ 100 to 200 km , CO_2^+ is overtaken by O^+ as the third-densest species, which is primarily produced via dissociative ionization of O_2 . As with its neutral counterpart (see Figure 3), the CO_2^+ density falls off sharply with altitude, becoming the fifth-densest ion species by

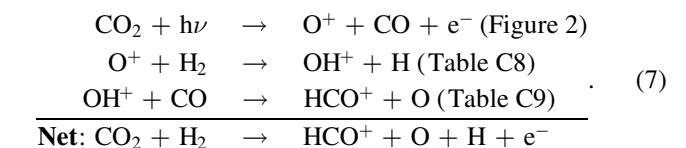
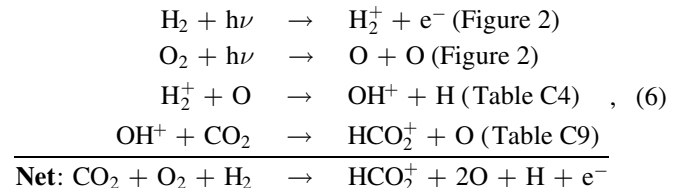
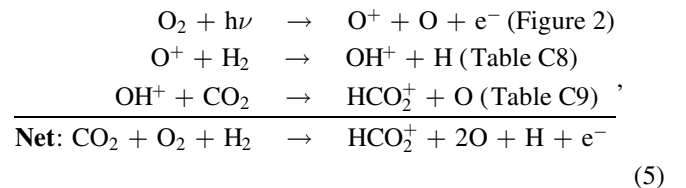
the C/A altitude of Juice; however, it is still detectable at such heights and continues to be so up to $\sim 290 \text{ km}$, above which, like HCO_2^+ , it can only be detected by JDC. The density of O^+ does not fall off as sharply and remains detectable up to $\sim 400 \text{ km}$ by NIM and from ~ 400 to 500 km only by JDC.

Below $\sim 50 \text{ km}$, the density of HCO^+ falls within CO_2^+ and O^+ , making it the fourth-densest species in Callisto's ionosphere close to the surface. Similar to O^+ , the peak in HCO^+ density occurs above the surface. HCO^+ is also similar to HCO_2^+ in that its lifetime is primarily limited by DR, and it is produced via several ion-neutral chemical reactions involving carbon- and hydrogen-bearing ions and neutrals; e.g.,



The density of HCO^+ drops off sharply after the altitude at which it peaks, so that it only exceeds the NIM density threshold up to $\sim 450 \text{ km}$; however, its energy exceeds the NIM upper limit by $\sim 330 \text{ km}$, above which it can only be detected by JDC.

H_2O^+ and OH^+ are solely produced in this photochemical model as a result of ion-neutral reactions; i.e., neutral H_2O and OH are not considered in the DSMC model. The photochemical production of OH^+ leads to several interesting outcomes (Table C9): it reacts with neutral H_2 to produce H_2O^+ ; it produces O_2^+ by reacting with O or exchanging its charge with O_2 , also resulting in neutral OH ; and it contributes further to the production of HCO_2^+ and HCO^+ via the following reaction pathways:



Upon production, H_2O^+ , in turn, can react with H_2 to produce H_3O^+ or exchange its charge with O_2 to produce O_2^+ as well as neutral H_2O (Table C6). The lone reaction for H_3O^+

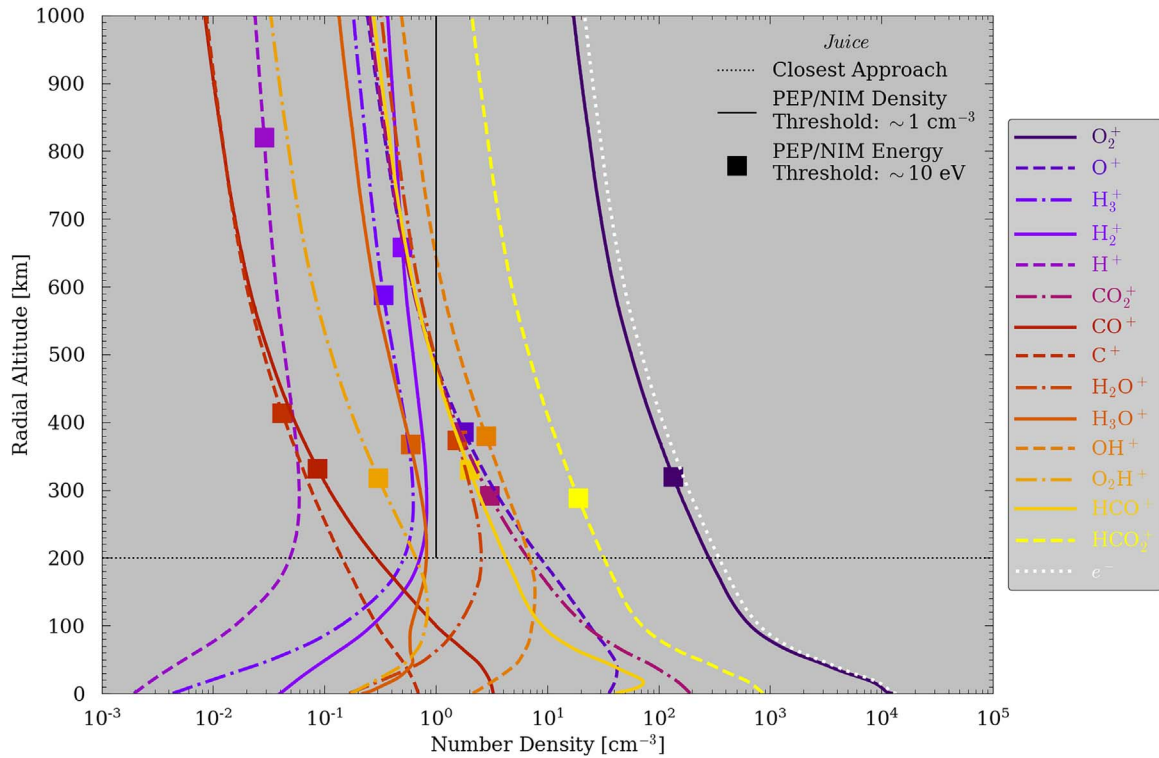


Figure 4. Results from the photochemical model of Callisto’s ionosphere at SZA = 0°, with inputs taken from DSMC models of Callisto’s neutral atmosphere (Figure 3), which is ionized by interactions with photons only. We also list the expected Juice C/A altitude (200 km) as well as the density and energy thresholds for its PEP/NIM instrument, $\sim 1 \text{ cm}^{-3}$ and 10 eV, respectively.

is DR, which, depending on the branching ratio, results in additional neutral OH or H₂O (Table C1). The densities of OH⁺ and H₂O⁺ initially increase with altitude, peaking around $\sim 100\text{--}200$ km such that they are actually detectable by Juice. Indeed, by ~ 250 km, the density of OH⁺ surpasses those of CO₂⁺ and O⁺. Similarly, by around ~ 300 km, H₂O⁺ has a density comparable to HCO⁺, and by around ~ 500 km to CO₂⁺ and O⁺. Given their similar mass, H₂O⁺ and OH⁺ remain detectable by NIM up to ~ 375 km and from there to ~ 500 and ~ 600 km by JDC. Above these altitudes, only O₂⁺, HCO₂⁺, and the accompanying electrons are detectable by JDC. Similar to OH⁺ and H₂O⁺, the density of H₃O⁺ peaks around ~ 200 km, but it is slightly below the NIM density threshold.

As illustrated in Figure 4, several other ions are produced via photochemistry but with densities below the PEP/NIM detection threshold at the expected C/A altitudes of the Juice encounters. H₂⁺ is not detectable, despite H₂ being the dominant neutral species in Callisto’s atmosphere above ~ 150 km (Figure 3). Interestingly, there is sufficient chemistry between H₂ and H₃⁺ that H₃⁺ is produced at Callisto (Table C4). Although H₃⁺ is also not detectable, it can contribute to the production of other ions that are, such as HCO₂⁺, HCO⁺, OH⁺, and H₂O⁺ (Table C5). O₂H⁺ is produced as a result of ion–neutral chemistry involving H₂⁺ or H₃⁺ and O₂ (Tables C4 and C5) but is ultimately also not detectable. Since the densities of H₂⁺ and H₃⁺ are relatively low, so too is that of O₂H⁺. However, since neutral O₂ is so dense, O₂H⁺ is denser than H₂⁺ or H₃⁺ below ~ 200 km because of the more rapid ion–neutral chemical reactions involving O₂ than H₂. With increasing altitude, however, the density of the much heavier O₂H⁺ drops off at a more rapid rate than those of H₂⁺ and H₃⁺, so the latter two species eventually dominate the former. Ionospheric H⁺ is

primarily produced via dissociative ionization of H₂, and it is the least dense species at the surface and remains so up to ~ 350 km, where its density eventually surpasses that of C⁺; at around ~ 400 km, its density also surpasses that of CO⁺. CO⁺ and C⁺ are largely produced via dissociative ionization of CO₂, and additional CO⁺ is produced from charge exchange (Tables C4 and C8) and ion–neutral chemistry involving C⁺, O₂, and CO₂ (Table C11). Although H⁺, C⁺, and CO⁺ may not be detectable, they can contribute to the detectability of other ion species (e.g., HCO⁺ and O⁺) as well as the recycling of additional neutral species (e.g., Tables C3, C11, and C12).

4.2.1. Photo- and Magnetospheric Electron-impact Ionization

To constrain the role that the variable Jovian magnetospheric electron population near Callisto has on the underlying ionospheric structure, we explored four possible cases, where electrons have densities, n_e , of 0.1 cm^{-3} and 1 cm^{-3} and temperatures, T_e , of 40 eV and 400 eV. With $n_e = 0.1 \text{ cm}^{-3}$, magnetospheric electron-impact ionization is negligible compared with or at most comparable to photoionization for either T_e (Figure 2). Therefore, the case including only photoionization is representative of Callisto’s ionosphere for times when the local magnetospheric electron density minimizes, which occurs when the moon is located far above and below the Jovian plasma sheet (e.g., M. G. Kivelson et al. 2004). Alternatively, for times when Callisto is embedded within the plasma sheet, the magnetospheric electron density is increased by nearly an order of magnitude (e.g., F. M. Neubauer 1998), and the concomitant ionization and subsequent ion–neutral chemistry produce a more robust ionosphere at the moon. Indeed, as can be seen in Figure 5 (also see Figures 4 and D1 and D2 in Appendix D), when comparing the modeling results

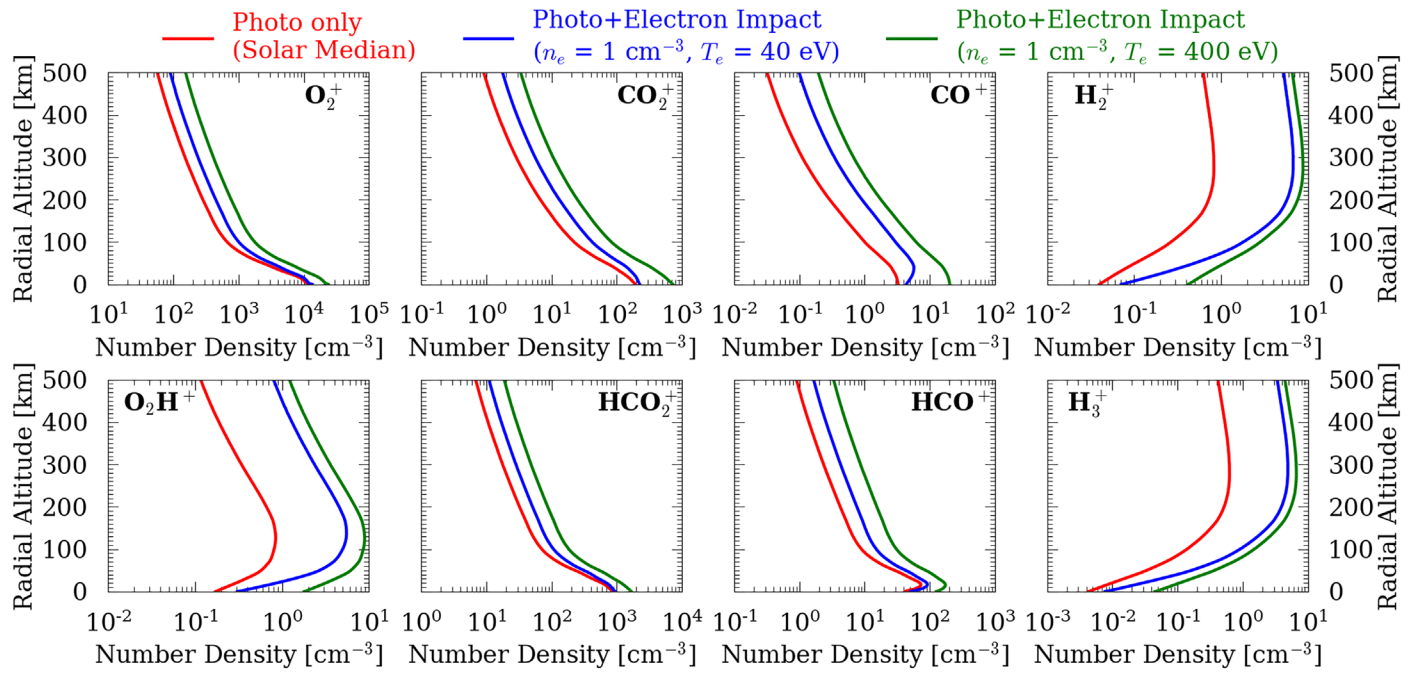


Figure 5. Comparison of results from photochemical modeling of Callisto’s ionosphere at SZA = 0° for O_2^+ , CO_2^+ , CO^+ , H_2^+ , O_2H^+ , HCO_2^+ , HCO^+ , and H_3^+ , where only interactions with photons were considered (red) and interactions with photons *and* magnetospheric electrons were considered an upstream density of $n_e = 1 \text{ cm}^{-3}$ and temperature of either $T_e = 40 \text{ eV}$ (blue) or $T_e = 400 \text{ eV}$ (green).

with and without including magnetospheric electron-impact ionization for the case with enhanced densities of $n_e = 1 \text{ cm}^{-3}$, all of the ion densities effectively increase when this additional source is included, resulting in several more species being detectable by Juice. In Figure 5, we focus on select ion species for comparisons between models with and without magnetospheric electron-impact ionization, whereas in Figures D1 and D2 in Appendix D, we illustrate all of the ion density profiles from the photochemical modeling carried out in this study.

Close to the surface, the results for the cases with photoionization only and photo- plus magnetospheric electron-impact ionization with $T_e = 40 \text{ eV}$ are similar because the impinging electrons’ energies are degraded with depth into the atmosphere (see Figures B1 and B2 in Appendix B). That is, as these electrons penetrate deeper into the atmosphere and their energies are reduced via collisions, the corresponding electron-impact ionization rates are diminished, and photoionization dominates close to the surface. Conversely, the electrons with $T_e = 400 \text{ eV}$ only deposit $\sim 10\%$ of their energy into the atmosphere (Figure B2 in Appendix B), so electron-impact ionization rates are not nearly as affected, and electron impacts remain the dominant source of the ionosphere. With increasing altitude from the surface, the results for the two cases with photo- and magnetospheric electron-impact ionization more closely resemble each other as energy deposition becomes less of a factor.

With $T_e = 40 \text{ eV}$, electrons contribute more to dissociation than ionization (see Figure 2), whereas with $T_e = 400 \text{ eV}$, the opposite is generally true except for ionization of H, where the rates are essentially the same for both T_e values because the electron-impact ionization cross sections do not vary much from ~ 20 – 1000 eV (Figure A5 in Appendix A). H_2 and H are ionized far more efficiently by electrons than photons (see Figure 2), so that H^+ , H_2^+ , and H_3^+ are more than an order of magnitude denser for either T_e . Similarly, since these densities are enhanced when magnetospheric electron ionization is

considered, so, too, are the densities of OH^+ , H_2O^+ , O_2H^+ , HCO_2^+ , and HCO^+ . An enhanced H_2O^+ results in a similarly enhanced H_3O^+ due to reactions with H_2 , and with larger H_3O^+ densities, more neutral OH and H_2O are produced via DR. Finally, given their relatively light mass and thus smaller energies corresponding to their magnetospheric pickup, H_2^+ and H_3^+ can remain detectable by NIM well above any other ion (Figures D1 and D2 in Appendix D).

4.2.2. Timescales

The ion densities presented by the photochemical model implemented in this study are a result of chemistry, diffusion, and magnetospheric pickup. Representative timescales are presented in Figure 6. Since the distribution of Callisto’s neutral atmosphere is negligibly affected by the inclusion of magnetospheric electron impacts (see Figure 3), the near-surface diffusion timescales, $\tau_D \sim H^2/D_A$, remain roughly the same throughout the three cases considered. On the other hand, the O_2^+ chemical loss timescale, $\tau_C = 1/(\alpha n_e)$, is noticeably affected, becoming shorter with increasingly efficient ionization mechanisms. Here $H = \sum_i (n(r)H(r))_i / \sum_i n_i(r)$ is the local mass-averaged atmospheric scale height, $D_A \sim 2 \times 10^{12} \text{ cm}^{-2} \text{ s}^{-1}$ is the ambipolar diffusion coefficient near the surface, α is the O_2^+ DR rate, and n_e is the ionospheric electron density. As can be seen in Figure 6, photochemistry is only efficient from the surface to ~ 35 – 45 km , where τ_C is the smallest timescale depending on the ionization mechanisms considered, photoionization with or without magnetospheric electron impacts, and the temperatures of the electrons, 40 eV or 400 eV. The pickup timescale, τ_{PU} , shown in Figure 6 is calculated as the time required for an ion to cross through the local H at the pickup speed taken from hybrid plasma models of Callisto’s local plasma environment (see Section 3.2) and becomes the smallest timescale above ~ 35 – 45 km . As with τ_D , τ_{PU} is effectively the same across the three cases considered.

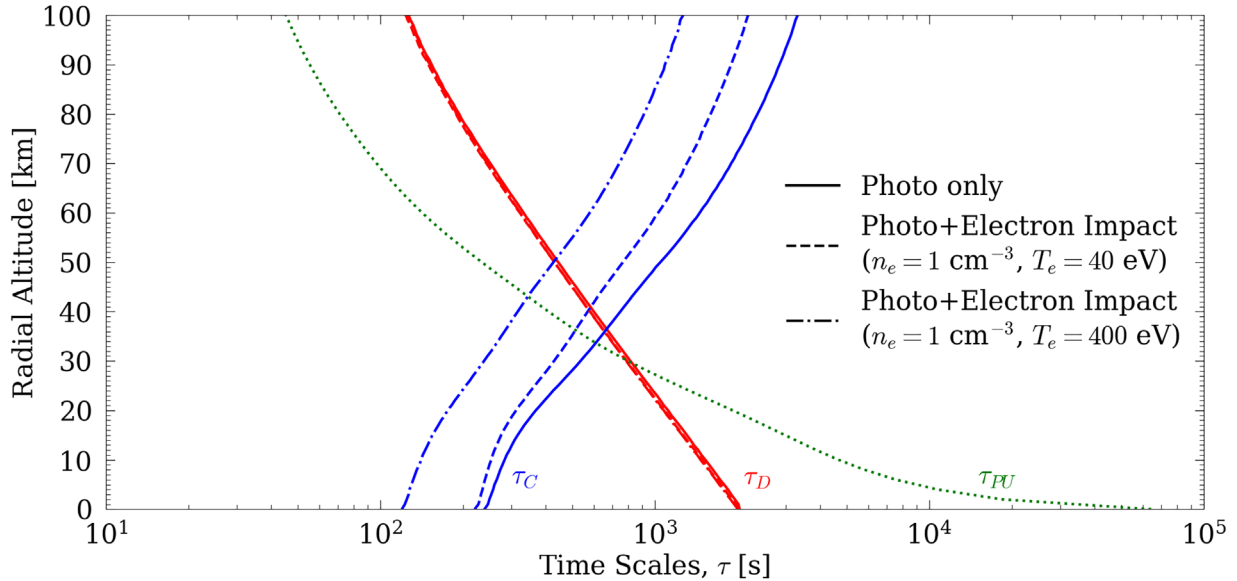


Figure 6. A comparison of timescales, τ , calculated in the photochemical model of Callisto’s ionosphere at $SZA = 0^\circ$ for photochemistry (τ_C), diffusion (τ_D), and magnetospheric pickup (τ_{PU}). Results for τ_C and τ_D are given for the three considered models, where only interactions with photons were considered (solid lines); and interactions with photons and magnetospheric electrons were considered, where at the top of the atmosphere the latter was assumed to have a density of $n_e = 1 \text{ cm}^{-3}$ and temperature of either $T_e = 40 \text{ eV}$ (dashed lines) or $T_e = 400 \text{ eV}$ (dashed-dotted lines). Only one line is shown for τ_{PU} because the results were effectively the same across all three cases considered.

Typically, PCE is defined when $\tau_C \ll \tau_D$, where \ll implies less than a factor of 10. Our results suggest that PCE only holds up to $\sim 10 \text{ km}$ above the surface when magnetospheric electron-impact ionization is considered with $n_e = 1 \text{ cm}^{-3}$ and $T_e = 400 \text{ eV}$. Transport due to ambipolar diffusion appears to be more important than that due to magnetospheric pickup below $\sim 30 \text{ km}$ (i.e., $\tau_{PU} > \tau_D$). However, both transport timescales are close enough to τ_C that neither can be ignored. Thus, given this limited altitude range where chemistry dominates—even in the case of an enhanced magnetospheric electron population ($n_e = 1 \text{ cm}^{-3}$, $T_e = 400 \text{ eV}$)—transport must be taken into account when modeling Callisto’s ionosphere.

5. Discussion

5.1. Comparison to Galileo

In Figure 7, we compare the electron densities from our photochemical model of Callisto’s ionosphere to those inferred from Galileo observations, specifically the detections made by PWS (D. A. Gurnett et al. 2000) and via radio occultations (A. J. Kliore et al. 2002). Whereas the data from the radio occultations are from individual observations entering and exiting the terminator regions during the C20, C22, and C23 flybys, the plasma-wave data are from a single flyby (C10), which occurred over the dayside in Callisto’s geometric wake. For the radio occultations, electron densities were inferred to be consistently $> 10^3 \text{ cm}^{-3}$, even with the lower limits provided by the error bars, and in two instances $> 10^4 \text{ cm}^{-3}$ (entry of Callisto’s shadow during the C22 and C23 flybys). Whereas the electron densities inferred from radio occultations represent measurements along the spacecraft’s line of sight (LOS)—enabling observations at altitudes below C/A—the electron densities inferred from plasma-wave detections during the C10 flyby correspond to in situ measurements at altitudes well above the surface with a C/A of 535 km (Figure 7). The electron densities inferred while Galileo was inbound peaked at $\sim 1200 \text{ km}$ and were larger than

those at C/A and during the outbound leg. For detections at C/A and as Galileo was outbound, electron densities were inferred to be generally $\gtrsim 10^2 \text{ cm}^{-3}$ below $\sim 800 \text{ km}$ before dropping off further with increasing altitude. We only present the inferred electron densities from the C10 flyby below $\sim 1000 \text{ km}$, the upper boundary of the photochemical model. Note that we do not consider the C3 flyby from which electron densities were inferred from plasma-wave detections (D. A. Gurnett et al. 1997), since the C/A was above the upper limit of the photochemical model, nor do we consider the radio occultation during the egress of the C22 flyby, because the reported error bars were larger than the inferred peak electron density.

We find that our simulated electron densities compare favorably to the electron densities inferred along the outbound leg of the C10 flyby. Since in our model, the plasma density gradients at high altitudes are primarily governed by the imposed pickup velocities, a shallower velocity gradient could enhance topside plasma densities, potentially bringing them even closer to the Galileo PWS measurements. The simulated electron densities also fit reasonably well to those inferred from the radio occultations. Since our model is 1D and inherently cannot capture the spatial variation of the ionospheric density in three dimensions as seen by Galileo, we caution against overinterpretation; however, the close agreement between our model and the outbound data represents the first time, within reasonable agreement, that both the observations made by PWS and by radio occultations have been simultaneously reproduced. We do note that the simulated electron densities underestimate the inbound observations at $\sim 800 \text{ km}$ and higher (see blue squares in Figure 7). We also note that full 3D hybrid modeling conducted by L. Liuzzo et al. (2016) also underestimated electron densities in this region (see their Figure 3). L. Liuzzo et al. (2016) explored the possibility that this data-model discrepancy could be the result of a regional atmospheric asymmetry; however, the strength of the asymmetry required to match the Galileo PWS measurements far exceeded known values for Callisto’s atmospheric density and thus was not

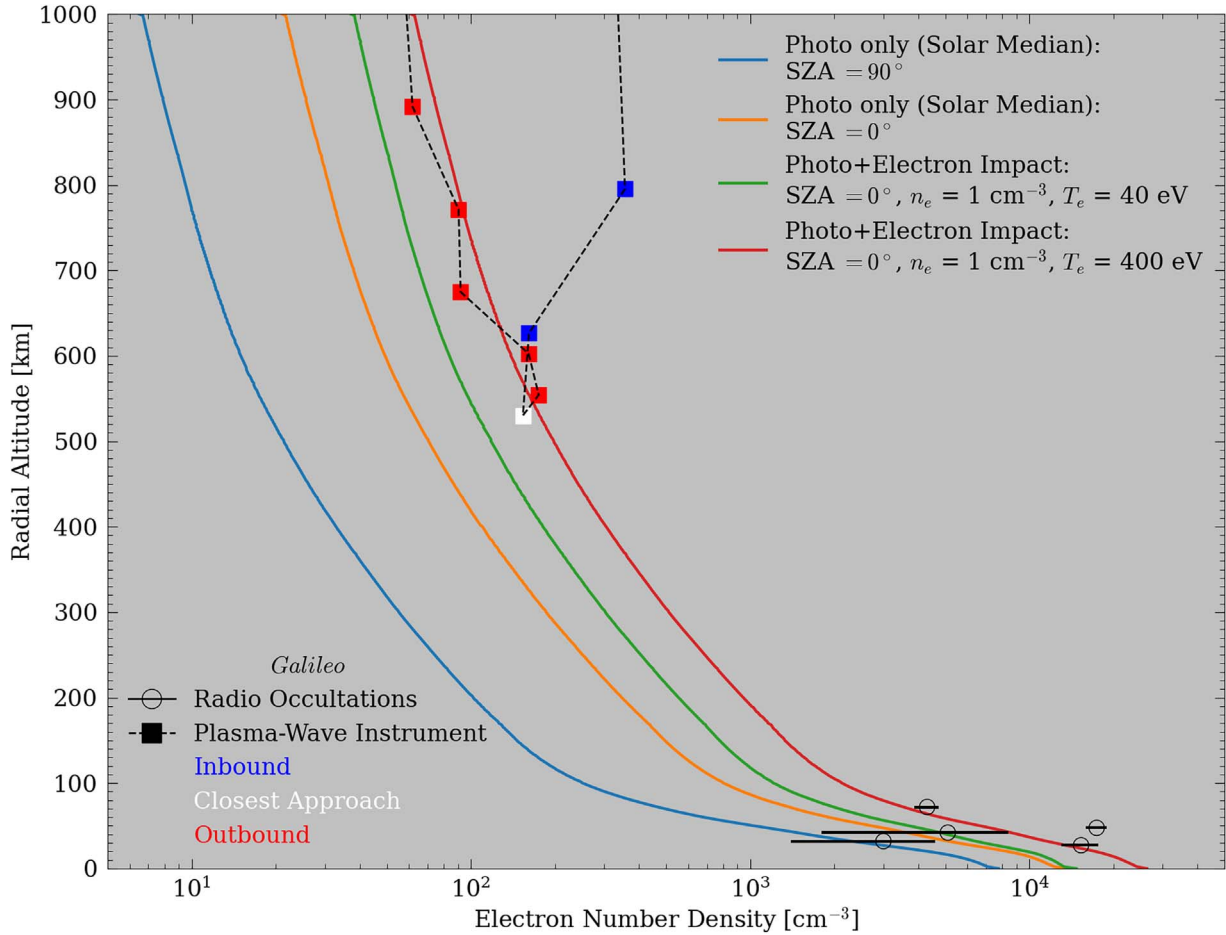


Figure 7. Electron densities from the photochemical model of Callisto’s ionosphere compared to those inferred from Galileo observations by PWS during the C10 flyby (red, white, and blue squares; D. A. Gurnett et al. 2000) and from radio occultations during the C20, C22, and C23 flybys (open black circles with horizontal lines representing error bars; A. J. Kliore et al. 2002). Electron densities in the photochemical model of Callisto’s ionosphere are calculated as the sum of all ion densities. The four considered models shown are for when only interactions with photons were considered (“Photo Only”) at SZA = 90° (blue) and 0° (orange) and when interactions with photons and magnetospheric electrons were considered (“Photo+Electron Impact”) at SZA = 0°, where at the top of the atmosphere the latter was assumed to have a density of $n_e = 1 \text{ cm}^{-3}$ and temperature of either $T_e = 40 \text{ eV}$ (green) or $T_e = 400 \text{ eV}$ (red).

considered a robust explanation. Future work is required to better constrain Callisto’s local magnetospheric plasma environment and its variability, so that magnetospheric electron-impact ionization and the corresponding ionospheric production in multiple dimensions can be more accurately modeled.

In order to reproduce the electron densities inferred along the spacecraft’s LOS during radio occultations, A. J. Kliore et al. (2002) suggested that a spherically symmetric O₂ component with surface and column densities on the order of $\sim 10^{10} \text{ cm}^{-3}$ and $\sim 10^{16} \text{ cm}^{-2}$, respectively, was required, values that have since conflicted with more recent (remote) observations (N. J. Cunningham et al. 2015; K. de Kleer et al. 2023) and models (S. R. Carberry Mogan et al. 2022) of Callisto’s atmosphere (see Section 2). In this study, consistent with S. R. Carberry Mogan et al. (2022), we implement an O₂ surface density of 10^9 cm^{-3} , which we show is also capable of reproducing the large electron densities inferred from radio occultations, providing even more evidence that Callisto’s O₂ atmosphere is not as dense as inferred by A. J. Kliore et al. (2002). Instead, O₂ surface and column densities on the order of $\sim 10^9 \text{ cm}^{-3}$ and $\sim 10^{15} \text{ cm}^{-2}$, respectively, are likely given these independent observational constraints and complementary modeling results. In order to make their calculations for the

required neutral densities, in addition to assuming a spherically symmetric atmosphere and ionosphere, A. J. Kliore et al. (2002) assumed that the atmosphere and ionosphere were in PCE, which we show in Figure 6 does not fully occur at Callisto.

5.2. Comparison to Previous Models

In Figure 8, we compare results from our model in which only photoionization is considered as the external ionization mechanism to that of M.-C. Liang et al. (2005). Whereas our model simulates Callisto’s atmosphere and ionosphere at solar median and at SZA = 0° and 90°, their model simulates solar maximum at SZA = 80°. At SZA = 0°, Callisto’s atmosphere is optically thin, so that the peak photoionization rates occur at the surface. However, with increasing SZA, the column density of a spherically symmetric atmosphere increases along an LOS because the path length through the atmosphere becomes longer and includes denser regions at lower altitudes, leading to photoabsorption that can become nonnegligible near the terminator (e.g., see Figure 7 in S. R. Carberry Mogan et al. 2022), potentially resulting in maximum photoionization rates occurring above the surface. In addition to the different SZA and solar activity implemented, there are several other key

differences between the model presented here and that of M.-C. Liang et al. (2005).

As can be seen in Figure 8, the ion and neutral densities modeled by M.-C. Liang et al. (2005) fall off sharply by ~ 200 km. In contrast, our modeled ion and neutral densities have much more gradual profiles and thus reach higher altitudes in greater quantities. This difference is due to our photochemical model simulating magnetospheric pickup of the ions and our DSMC model simulating nonthermal collisions. Without including such phenomena, the model of M.-C. Liang et al. (2005) would suggest that O_2 , CO_2 , O_2^+ , CO_2^+ , and O^+ are *not* detectable by Juice/PEP/NIM above C/A and only O would be with densities just barely exceeding its detection threshold, contrary to our results suggesting that all of these species should be readily detectable.

The photochemical framework considered by M.-C. Liang et al. (2005) was relatively limited compared to ours; e.g., their model only considered two ion–neutral reactions: charge exchange between CO^+ and O_2 and between H_2O^+ and O_2 (Table 1 therein; see Tables C3–C19). The model of M.-C. Liang et al. (2005) implemented an O_2 surface density even larger than that inferred by A. J. Kliore et al. (2002), which was $\sim 10\times$ denser than what we implemented. Due to the suppression of photoionization in an optically thick atmosphere, resulting from this much denser O_2 component and higher SZA, the model of M.-C. Liang et al. (2005) yields similar peak O_2^+ densities to ours (Figure 8), on the order of $\sim 10^4 \text{ cm}^{-3}$. Another stark difference is that we did not include sublimated H_2O , which was considered by M.-C. Liang et al. (2005). M.-C. Liang et al. (2005) assumed that Callisto’s average dayside surface temperature was 150 K so that sublimation can still efficiently occur at SZA = 80° . However, observations by Voyager 1 and 2 and Galileo suggest that Callisto’s surface temperature drops off rapidly with increasing distance from the subsolar point (e.g., see Figure 1 in S. R. Carberry Mogan et al. 2022), so that the average dayside surface temperature is much smaller. Moreover, sublimation rates drop off exponentially with increasing SZA and the corresponding decrease in surface temperature, so that at least a 2D model is required to accurately represent sublimated H_2O in Callisto’s atmosphere, which would have an exceedingly low density at SZA = 80° (e.g., S. R. Carberry Mogan et al. 2021b, 2022). The model of M.-C. Liang et al. (2005) initially predicted such a large O density that water vapor had to be introduced in order to inhibit the buildup of O so that it did not exceed the upper limits set by D. F. Strobel et al. (2002). However, since the sublimated water vapor they simulated was more than 2 orders of magnitude larger than the upper limits set by S. R. Carberry Mogan et al. (2022), with a much less dense H_2O component, the model of M.-C. Liang et al. (2005) will also predict too-large O densities.

O. Hartkorn et al. (2017) demonstrated that a peak in electron densities above the surface viewed along Galileo’s LOS during radio occultations can occur in an *asymmetric* atmosphere and ionosphere (see Figures 13 and 14 therein). Since the production and corresponding distribution of Callisto’s atmosphere vary as a function of the diurnal surface temperature gradient (e.g., S. R. Carberry Mogan et al. 2021b, 2022), Callisto’s ionosphere should also be asymmetric, driven largely by the same diurnal variations as well as interactions with photons and magnetospheric electrons and the concomitant ion–neutral chemistry. Additionally, we show here

that ionization induced by magnetospheric electrons can dominate that by photons depending on their upstream densities and temperature as well as the extent to which their energy is degraded in the atmosphere, thereby affecting where the peak in electron density altitudes occurs. Thus, future work is required to simulate Callisto’s asymmetric atmosphere and ionosphere in multiple dimensions with better constraints on the precipitating magnetospheric electrons to determine where peak electron densities occur when viewed along an LOS during radio occultations.

S. R. Carberry Mogan et al. (2022) argued that the observation of enhanced electron densities during the C10 flyby (D. A. Gurnett et al. 2000) hundreds to thousands of kilometers above Callisto’s surface reaffirmed their notion that an extended H_2 component was present, as its ionization by solar photons and magnetospheric electron impacts could supply the detected electrons. While we still suggest that H_2 is indeed present in Callisto’s atmosphere, as evidenced by the morphology of its H corona, Figures 4 and D1 and D2 in Appendix D demonstrate that ionization of an extended H_2 component is not required to reproduce the cold electrons detected during the C10 flyby. H_2^+ is certainly produced the most among the ions of Callisto’s ionosphere at such high altitudes, via direct ionization of H_2 , which is the densest neutral species above ~ 150 km (Figure 3). However, the magnetospheric pickup of O_2^+ , which is by far the densest ion near the surface, can explain the plasma-wave observations, consistent with earlier hybrid plasma models (L. Liuzzo et al. 2015, 2016). Indeed, our photochemical model of Callisto’s ionosphere demonstrates that O_2^+ remains the densest ion in the ionosphere up to ~ 1000 km despite the rapid dropoff in density of neutral O_2 .

Finally, while the DSMC model simulates multiple neutral species, particularly H_2 , and the photochemical model includes an even broader range of ion species, the AIKEF simulations of L. Liuzzo et al. (2015, 2016) only tracked O_2^+ and CO_2^+ . Although H_2 dominates at high altitudes, O_2 and CO_2 are 16 and 22 times more massive, respectively, meaning the mass and momentum loading of the bulk plasma due to H_2^+ pickup is negligible compared to that from O_2^+ and CO_2^+ . Consequently, any perturbations to the electromagnetic environment caused by H_2^+ (and H_3^+) are minimal relative to those driven by O_2^+ and CO_2^+ . Nevertheless, future AIKEF modeling can extend these studies by incorporating additional ion species (e.g., HCO_2^+ and H_2O^+) to investigate their magnetospheric pickup and associated mass-dependent gyromotion.

5.3. H_2O^+ and OH^+ (and H_3O^+) without Neutral H_2O and OH

Here, we refrained from simulating sublimated H_2O because we simulated Callisto’s atmosphere and ionosphere in 1D, and a 2D model is required to accurately describe Callisto’s diurnal surface temperature gradients and the influence this has on sublimation (e.g., S. R. Carberry Mogan et al. 2021b, 2022). For this same reason, we did not include OH in our models, which is primarily produced via dissociation of H_2O (e.g., W. F. Huebner & J. Mukherjee 2015). Surprisingly, however, H_2O^+ , OH^+ , and even H_3O^+ were produced via ion–neutral chemistry in sufficient amounts that they can be detected by Juice. Thus, a detection of these species does not necessarily imply that neutral water vapor or its dissociated product OH is present in large quantities in the atmosphere.

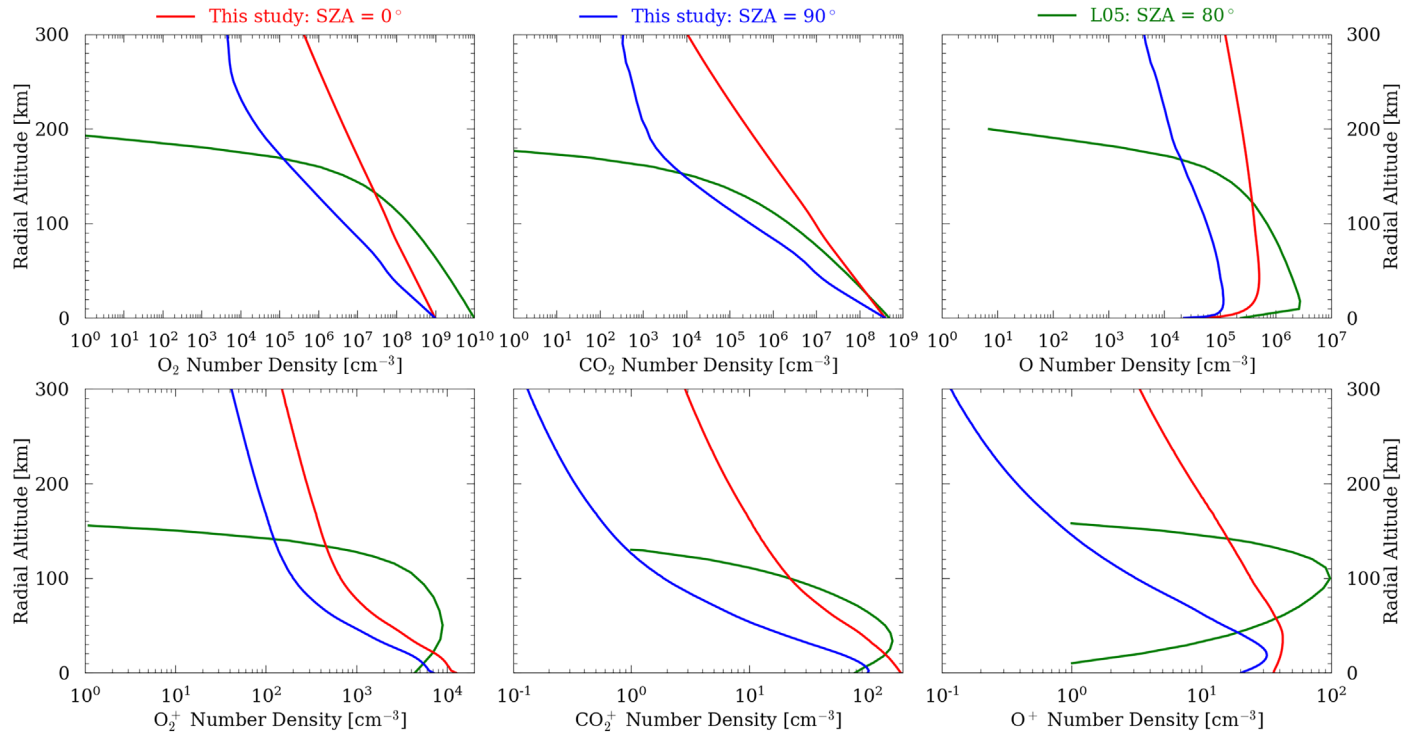
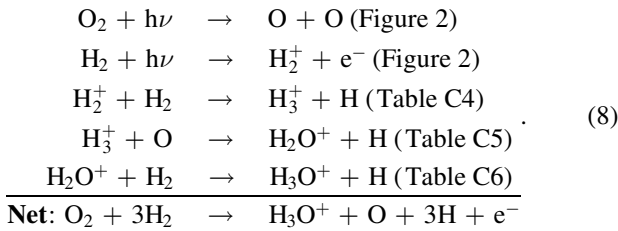


Figure 8. Results from our DSMC and photochemical models of Callisto’s atmosphere and ionosphere where only interactions with photons were considered at solar median and SZA = 0° (red) and 90° (blue) are compared to the results of the photochemical model of M.-C. Liang et al. (2005), “L05,” at solar maximum and SZA = 80° (green). Number density profiles are plotted for O₂ (top left panel), CO₂ (top center panel), O (top right panel), O₂⁺ (bottom left panel), CO₂⁺ (bottom center panel), and O⁺ (bottom right panel).

The results presented here for these ions can be seen as lower limits, because if there are neutral H₂O and OH components, then the accompanying ions should only be denser and the corresponding chemical reactions more frequent. For example, without H₂O in our model of Callisto’s neutral atmosphere, H₃O⁺ only forms via ion–neutral chemistry involving H₂O⁺ and H₂; e.g.,



However, with a neutral H₂O component also present, H₃O⁺ will directly and more rapidly form as a result of ion–neutral chemistry between neutral and ionized water vapor, similar to the chemistry between neutral and ionized H₂ leading to H₃⁺.

The ion–neutral chemical reactions that follow the production of OH⁺, H₂O⁺, and H₃O⁺ have profound implications for Callisto’s atmosphere: neutral OH and H₂O can be produced without a direct source, e.g., sublimation or sputtering of water ice, and dissociation of the corresponding water vapor leading to OH. However, we do not track the neutral species resulting from such photochemical reactions in the DSMC model because the coupling involved in this study is only one-way: from the DSMC to the photochemical model but not vice versa. Implementing two-way coupling between DSMC and photochemical models in order to simulate the resultant evolution of H₂O and OH is the subject of future work.

As mentioned earlier, upper limits were recently provided by S. R. Carberry Mogan et al. (2022) for sublimation fluxes and

the corresponding H₂O number and column densities. However, it is not known just how much H₂O can be expected in the atmosphere below these limits. Fortunately, forthcoming HST observations hope to shed light on this (L. Roth et al. 2024). A detection of H₂O can be used in subsequent multidimensional DSMC models to simulate its corresponding distribution, as well as that of OH, which can then be used as inputs for a photochemical model to determine how much, e.g., H₂O⁺, H₃O⁺, and OH⁺ can be expected in the ionosphere in preparation for Juice. Indeed, these studies are the subjects of future work following the forthcoming HST observations.

5.4. Callisto’s Carbon Cycle

When the CO particles simulated in the DSMC models presented herein returned to the surface, they were removed. However, CO is a highly volatile species and should, at the temperatures relevant to Callisto’s surface, continuously desorb from the surface, much like what is expected to happen for O₂, H₂, and, to a lesser extent, CO₂. Therefore, the results we present here for CO can be seen as lower limits because we effectively implement a unity sticking coefficient. Recent studies have considered surface trapping of volatiles such as CO on icy comets and have found sticking coefficients to be well below unity (N. F. W. Ligterink et al. 2024). Because our focus was on Callisto’s ionosphere, we did not explore this concept in greater detail. Future work will explore nonunity sticking coefficients for CO and the influence this has on its neutral density distribution. Additionally, in a two-way coupled DSMC and photochemical model, even more CO would be produced as a result of DR (Table C1), ion–neutral chemistry (Tables C8, C11, and C13), and charge exchange (Table C12). With a denser CO component, neutral C can be produced in

greater quantities via dissociative processes, possibly leading to amounts detectable by Juice. Moreover, CO^+ and C^+ will be produced in greater quantities—especially if ionization rates are enhanced by magnetospheric electron impacts—that have several ripple effects in the ion–neutral photochemical network between Callisto’s neutral atmosphere and ionosphere, enhancing the production of ions such as HCO^+ . Indeed, further exploration of this “carbon cycle” on Callisto will provide interesting insights into the coupled evolution of its atmosphere and ionosphere.

5.5. Implications for the Juno Flybys of Europa and Ganymede

Juno flew by Ganymede and Europa, and its onboard Jovian Auroral Distributions Experiment (JADE; D. J. McComas et al. 2017) detected ions indicative of the species present in their atmospheres as well as the ion–neutral chemistry, or lack thereof, occurring within their atmospheres and ionospheres.

P. W. Valek et al. (2022) present the ions detected by Juno/JADE during the flyby of Ganymede: H^+ , H_2^+ , H_3^+ , O^+ , and O_2^+ . As discussed above, H_3^+ is produced via ion–neutral chemistry, primarily between H_2 and H_2^+ . While H^+ , H_2^+ , O^+ , and O_2^+ provide direct evidence for their neutral counterparts, H_3^+ suggests that H_2 and H_2^+ are sufficiently dense at Ganymede that ionization and subsequent chemistry is efficient enough for a detectable amount of H_3^+ to be produced. As with our results at Callisto (Figures 4 and D1 and D2 in Appendix D), H_2^+ at Ganymede remains denser than H_3^+ , suggesting that H_2^+ tends to react with Ganymede’s O_2 component, leading to O_2H^+ . Given the mass resolution of Juno/JADE in this mass range (D. J. McComas et al. 2017), however, O_2H^+ is likely difficult to discern from O_2^+ . A detection of O_2H^+ would provide evidence for ion–neutral chemistry between H_2^+ and O_2 , which should be expected since both are present in Ganymede’s ionosphere and atmosphere, respectively.

The mass resolution of JADE is also likely why OH^+ , H_2O^+ , and/or H_3O^+ could not be distinguished from O^+ , although H_2O is expected to be present in Ganymede’s atmosphere (L. Roth et al. 2021), albeit primarily above the subsolar point, where sublimation is most efficient. Thus, with a higher mass resolution, any lack of detections would instead be indicative of H_2O not being efficiently ionized where the Juno flyby occurred, which was over the terminator. Indeed, any ionization of sublimated H_2O would primarily occur in the closed field line region (e.g., M. L. Marconi 2007), which Juno did not enter (S. Duling et al. 2022). Similarly, although H_2O can be produced globally as a result of sputtering (e.g., F. Leblanc et al. 2017), a nondetection would suggest that sputtered H_2O and any resulting ions (e.g., H_2O^+ , H_3O^+ , and/or OH^+) may not reach outside Ganymede’s magnetosphere.

JWST recently detected CO_2 in Ganymede’s atmosphere (D. Bockelée-Morvan et al. 2024). However, again likely due to instrument sensitivity in this mass range, CO_2^+ was not detected by Juno/JADE. Also not detected were HCO^+ and HCO_2^+ , which we show here are produced at Callisto as a result of ion–neutral chemistry between neutral and ionized H , H_2 , and CO_2 , all of which are present at Ganymede. However, as with a nondetection of H_2O -related ions, the Juno flyby may not have provided a favorable trajectory to detect CO_2 -related ions, since JWST showed that CO_2 tended to remain in the polar region. Nevertheless, based on the findings presented here at Callisto, and since Ganymede has a similar atmospheric and

ionospheric composition, the detection of CO_2^+ as well as HCO_2^+ , and possibly even HCO^+ , is likely given the mass resolution of Juice ($\Delta m/m \sim 500$), which will fly by Ganymede many times at much closer C/A altitudes, covering a more extensive area.

Juno also flew by Europa, where its JADE instrument detected H^+ , H_2^+ , and O_2^+ (J. R. Szalay et al. 2024), providing further evidence for its neutral H (L. Roth et al. 2017b) and O_2 (L. Roth et al. 2016) components, as well as the first direct evidence for its H_2 component, which has thus far only been suggested to be present as the primary source of its neutral torus (W. H. Smyth & M. L. Marconi 2006; H. T. Smith et al. 2019) and H corona (L. Roth et al. 2023). However, unlike what was observed at Ganymede or modeled here at Callisto, H_3^+ was not detected at Europa, suggesting that the H_2 and/or corresponding H_2^+ components are not dense enough for ion–neutral chemistry to occur efficiently. This is consistent with the H_2 density inferred by J. R. Szalay et al. (2024), which is ~ 2 orders of magnitude smaller than that implemented here at Callisto, which was found to be capable of reproducing its H corona (S. R. Carberry Mogan et al. 2022), and similarly less dense than the H_2 component inferred from the Juno flyby of Ganymede required to reproduce the detected H_2^+ and H_3^+ (e.g., J. H. Waite et al. 2024; see Figures 8 and 9 therein) and required to reproduce the $\text{Ly}\alpha$ emissions observed by Galileo’s UV spectrometer (C. A. Barth et al. 1997; M. L. Marconi 2007). An alternative or complementary explanation could be that, unlike Callisto, where chemistry can only efficiently occur up to ~ 40 km (Figure 6), diffusion and pickup dominate throughout Europa’s ionosphere so that all nascent ions are rapidly swept away by the corotating Jovian magnetosphere, thereby inhibiting ion–neutral chemistry.

6. Conclusion

Here we present a photochemical model of Callisto’s ionosphere with inputs supplied by a DSMC model of its neutral atmosphere. We compare a model that considers interactions with photons as the sole external ionization mechanism to models that also include magnetospheric electron impacts, where a range of upstream electron densities and temperatures are considered. With an upstream density of $\sim 1 \text{ cm}^{-3}$, magnetospheric electron impacts dominate the production of Callisto’s ionosphere, while below this density, photoionization is the dominant external ionization mechanism. Depending on the upstream electron temperature, which we vary from 40 to 400 eV, electrons either more efficiently dissociate molecules than photons (40 eV), leading to enhanced production of nonthermal neutral species, such as H , O , and CO , or are far more efficient at ionizing molecules than dissociating them (400 eV), leading to enhanced ionospheric production and subsequent ion–neutral chemistry.

In order to provide a more accurate description of how efficiently magnetospheric electrons deposit their energy into and ionize the atmosphere, as well as dissociate molecules producing nonthermal species, upstream plasma conditions at Callisto’s orbit need to be better constrained. Nevertheless, the results presented here have significant implications for the forthcoming Juice flybys of Callisto, as we demonstrate that several ion species that are produced via complex photochemistry can be detected according to the spacecraft’s instrumentation and expected C/A altitude.

We also compared the electrons produced in these simulations to those inferred from Galileo observations, yielding novel results. We demonstrated that ionization of an O₂ component with a surface density of 10⁹ cm⁻³ is capable of producing the electron densities detected during radio occultations (A. J. Kliore et al. 2002), from which an order-of-magnitude denser O₂ was initially inferred. Thus, we have provided even more evidence that O₂ is *not* as dense as was suggested following the Galileo mission. The electron densities were also compared with those inferred from Galileo observations of plasma waves (D. A. Gurnett et al. 2000), demonstrating reasonable agreement up to \sim 1000 km. Thus, we have presented the first model capable of simultaneously reproducing both the radio occultations observed close to and plasma-wave observations hundreds of kilometers above Callisto's surface.

The implications of this work also highlight several interesting studies that can be explored in future work.

We show that H₂O⁺ and OH⁺ can be present despite not having modeled neutral H₂O and OH. Forthcoming HST observations of Callisto's atmosphere hope to detect H₂O therein (L. Roth et al. 2024), which will provide the necessary inputs for a multidimensional DSMC model to simulate its corresponding distribution as well as that of its dissociated product OH. These results can then be fed into a photochemical model, where the resultant enhanced H₂O⁺ and OH⁺ densities as well as those of H₃O⁺ and possibly other ions can be estimated.

Here we assumed that all CO particles produced via photodissociation of CO₂ stick on return to the surface in the DSMC models of Callisto's atmosphere. Thus, our results can be interpreted as lower limits for CO because it is known to be a highly volatile species. Based on these lower limits, future Juice observations should be able to detect CO, which can be used to constrain the corresponding sticking efficiency. In the meantime, however, a range of sticking efficiencies can be explored, guided by, e.g., experimental work for icy comets (N. F. W. Ligerink et al. 2024), to determine the influence this

has on the resultant CO distribution. Moreover, any enhancement in neutral CO will lead to more neutral C, as well as CO⁺, C⁺, and several other ions via photochemistry. Since CO₂ has been detected in Callisto's atmosphere, CO must also be present; and if CO is present, then so, too, is C. Determining how dense these species are prior to the arrival of Juice can guide the forthcoming observations.

Another limitation of the presented models is that they were one-way coupled; i.e., the DSMC modeling results were fed into the photochemical model but not vice versa. Future work will look to create two-way coupling between DSMC and photochemical models. This coupling would result in non-thermal sources for the neutral atmosphere in addition to those considered here, e.g., recycling of species via charge exchange, as well as ion–neutral chemistry and DR of molecular ions. Such photochemical reactions can also result in new neutral species (e.g., H₂O and OH) that were not originally included in the DSMC model. Nevertheless, the one-way coupling between a DSMC and a photochemical model presented here provides key insights into the interplay between Callisto's neutral atmosphere and ionosphere, offering a robust framework to expand upon for better interpreting Galileo observations and informing future studies in anticipation of the Juice mission.

Acknowledgments

S.R.C.M., L.L., and A.R.P. acknowledge support from NASA Solar System Workings grants 80NSSC21K0152 and 80NSSC22K0097. L.M. acknowledges support from NASA New Frontiers Data Analysis Program grant 80NSSC23K0661.

Appendix A Electron-impact Collision Cross Sections

Figures A1–A5 illustrate the electron-impact collision cross-section distributions implemented in this study to determine the corresponding reaction rates.

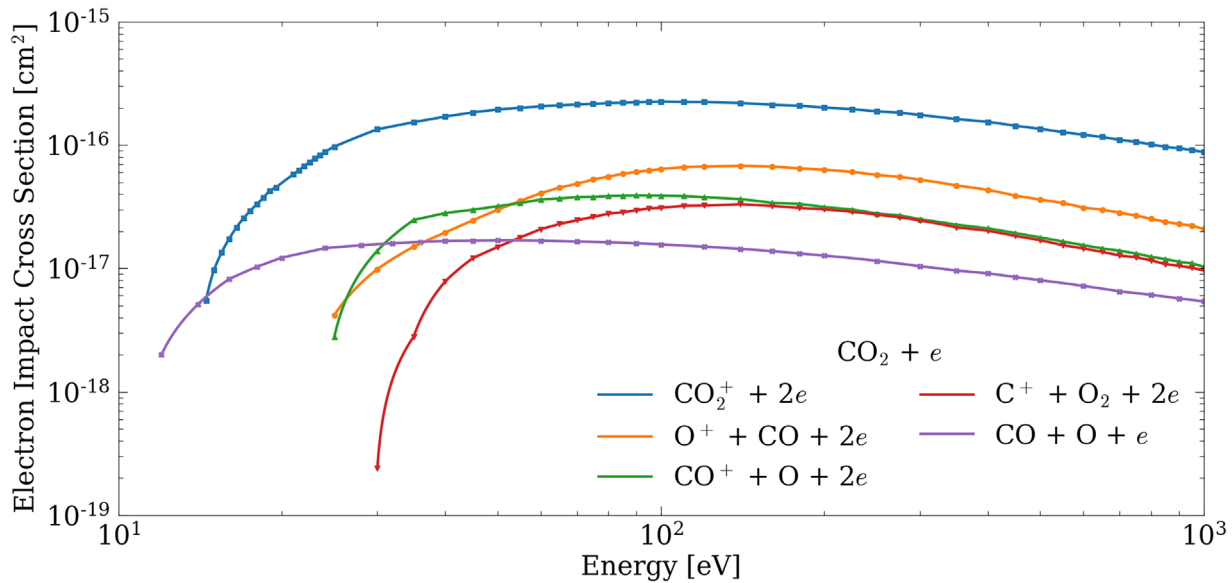


Figure A1. Collision cross sections for electrons impacting CO₂ (y-axis) as a function of energy (x-axis). These electron-impact cross sections are taken from Y. Itikawa (2002).

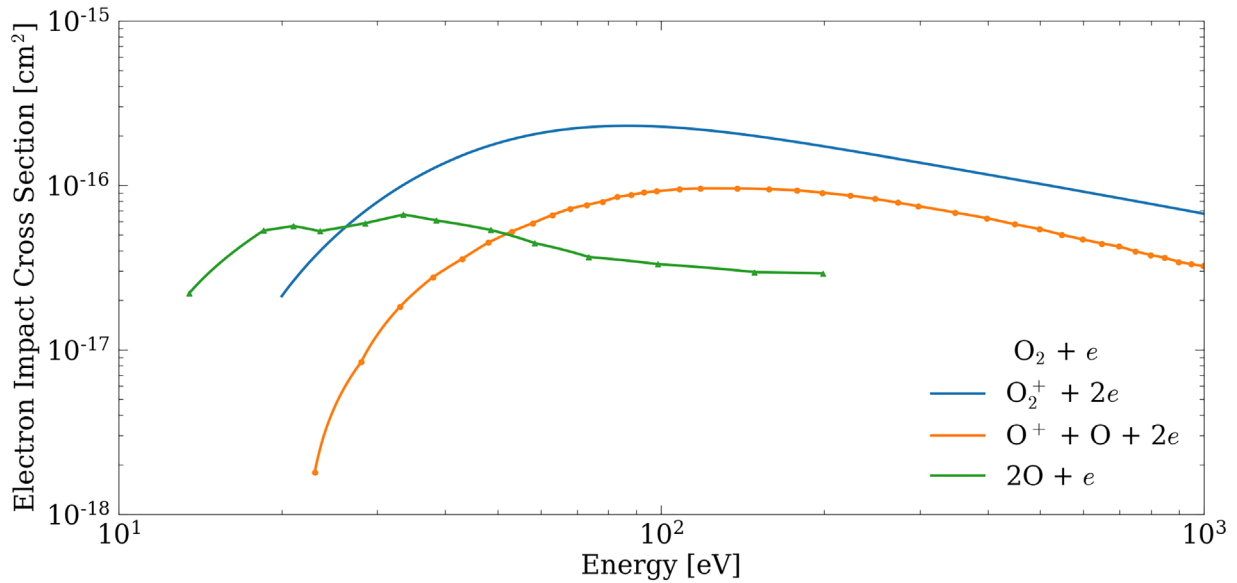


Figure A2. Collision cross sections for electrons impacting O_2 (y-axis) as a function of energy (x-axis). These electron-impact cross sections are taken from the following references: S. R. Carberry Mogan et al. (2023a) for $e + O_2 \rightarrow O_2^+ + 2e$, H. C. Straub et al. (1996) for $e + O_2 \rightarrow O + O^+ + 2e$, and P. C. Cosby (1993) for $e + O_2 \rightarrow 2O + e$.

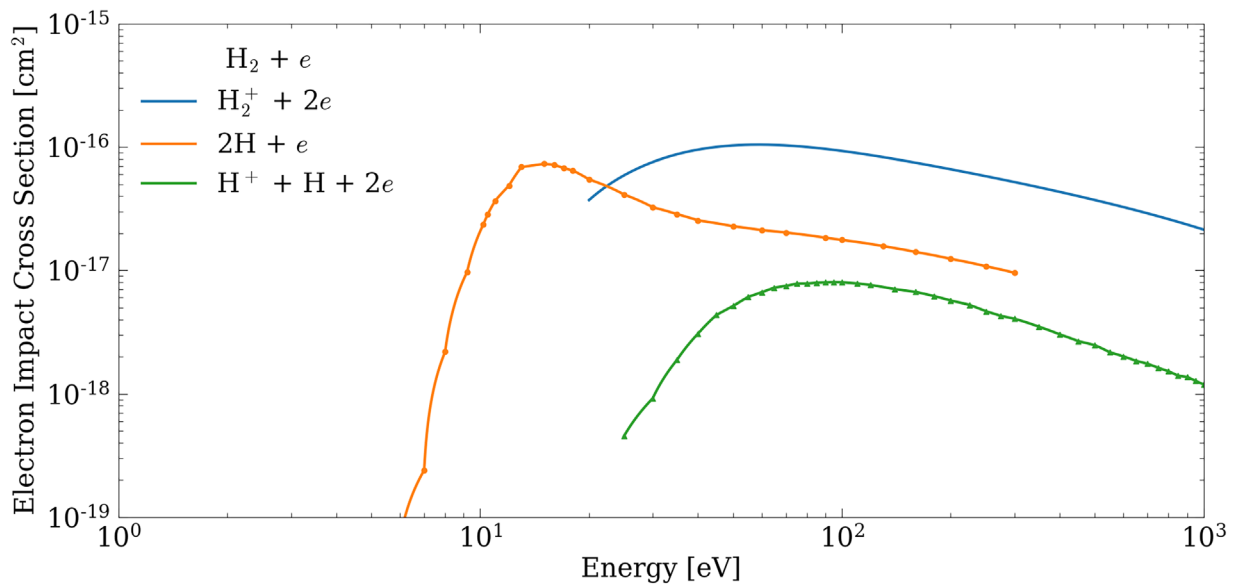


Figure A3. Collision cross sections for electrons impacting H_2 (y-axis) as a function of energy (x-axis). These electron-impact cross sections are taken from the following references: S. R. Carberry Mogan et al. (2023a) for $e + H_2 \rightarrow H_2^+ + 2e$, L. H. Scarlett et al. (2018) for $e + H_2 \rightarrow 2H + e$, and H. C. Straub et al. (1996) for $e + H_2 \rightarrow H + H^+ + 2e$.

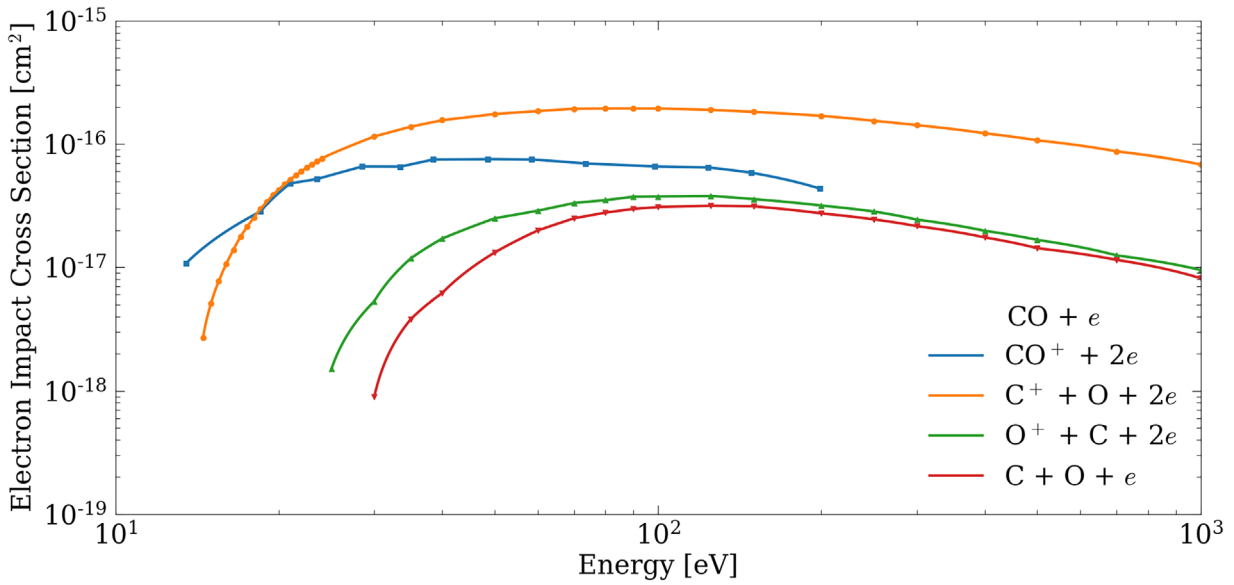


Figure A4. Collision cross sections for electrons impacting CO (y-axis) as a function of energy (x-axis). These electron-impact cross sections are taken from Y. Itikawa (2015).

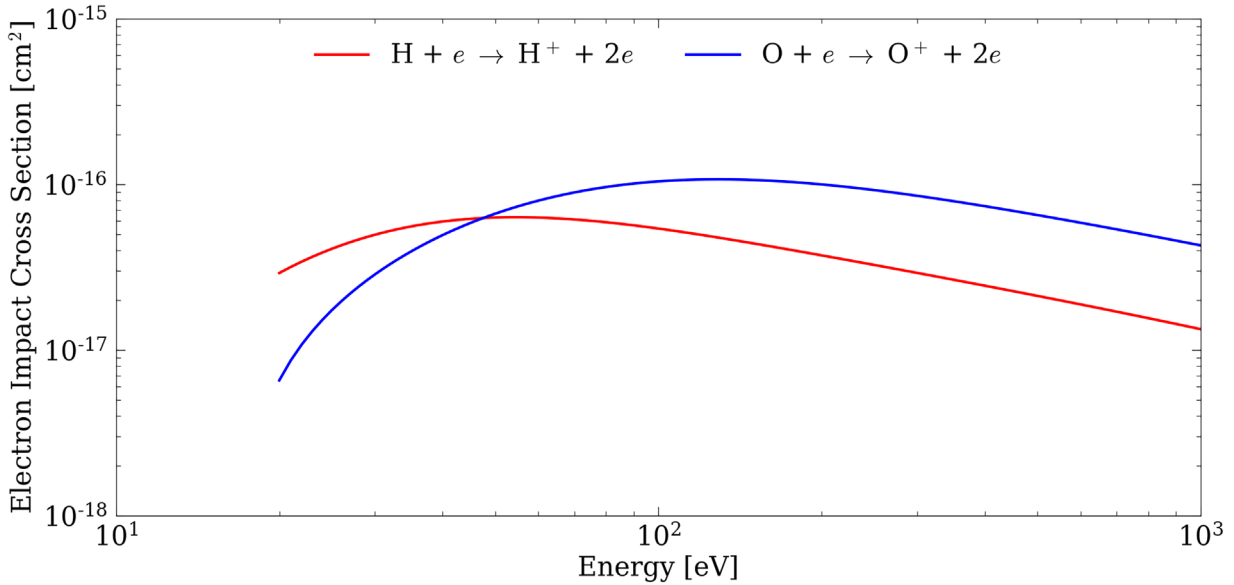


Figure A5. Electron-impact ionization cross sections (y-axis) for H (red) and O (blue) as a function of energy (x-axis). These electron-impact cross sections are taken from S. R. Carberry Mogan et al. (2023a).

Appendix B Energy Deposition

When simulating energy deposition in Callisto's atmosphere, we implement a similar approach as that by S. R. Carberry Mogan et al. (2023b). We first derive an energy distribution for electrons at the top of the atmosphere according to their temperature-defined Maxwellian distributions, which are illustrated in Figure B1. We assume the electrons penetrate the atmosphere radially inward, neglecting any asymmetries resulting from, e.g., the ram or wake region. We then calculate the degradation of each bin of the energy distribution using stopping cross sections (see Appendix C in S. R. Carberry Mogan et al. 2023b). The resultant energy calculated at the bottom of one cell is the

initial energy at the top of the cell below that, and so on until reaching the surface, where the final energies are calculated. By convolving these local energy distributions with the electron-impact collision cross sections listed in Appendix A, we are able to calculate a radial profile of the corresponding electron-impact reaction rates.

This reduction in energy can also be used to determine the number density of the electrons able to reach the surface without depositing all of their energy. In Figure B2, we show the ratio between this value and the number density of electrons at the assumed top of the atmosphere (1000 km). As can be seen, electrons with a temperature of 40 eV deposit much more of their initial energy before reaching the surface ($\sim 90\%$) than those with temperatures of 400 eV ($\sim 10\%$).

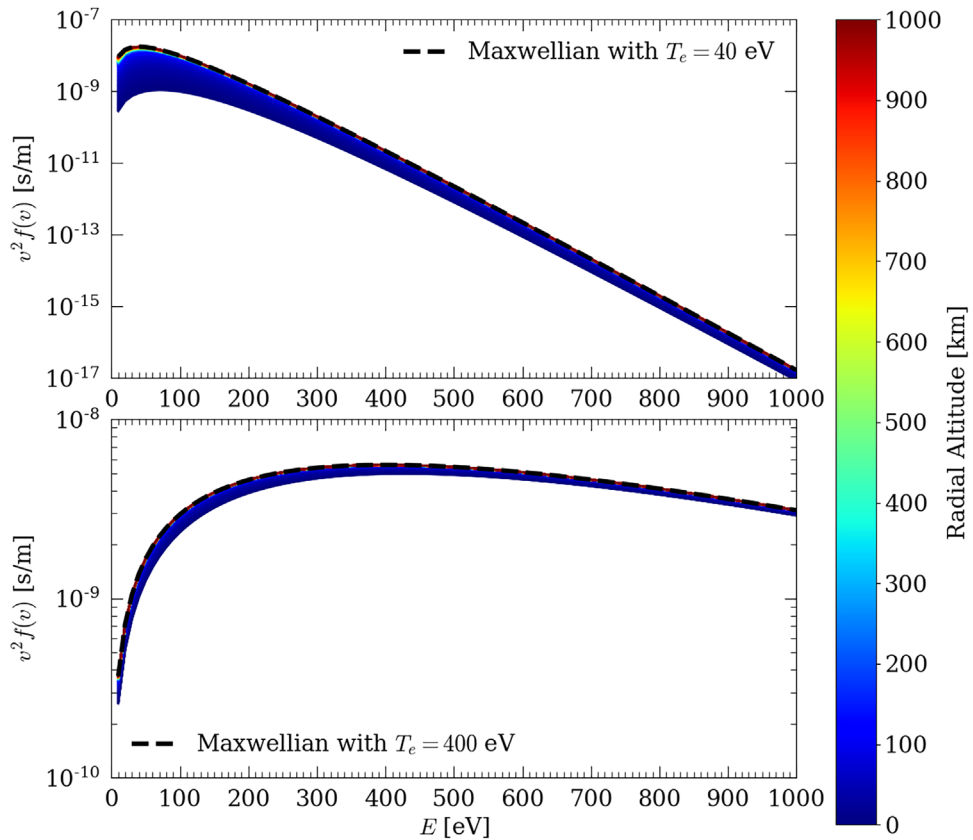


Figure B1. Maxwellian energy distributions for magnetospheric electrons with upstream temperatures of 40 eV (top) and 400 eV (bottom), calculated as a function of radial altitude above Callisto's surface based on the energy deposited in the atmosphere.

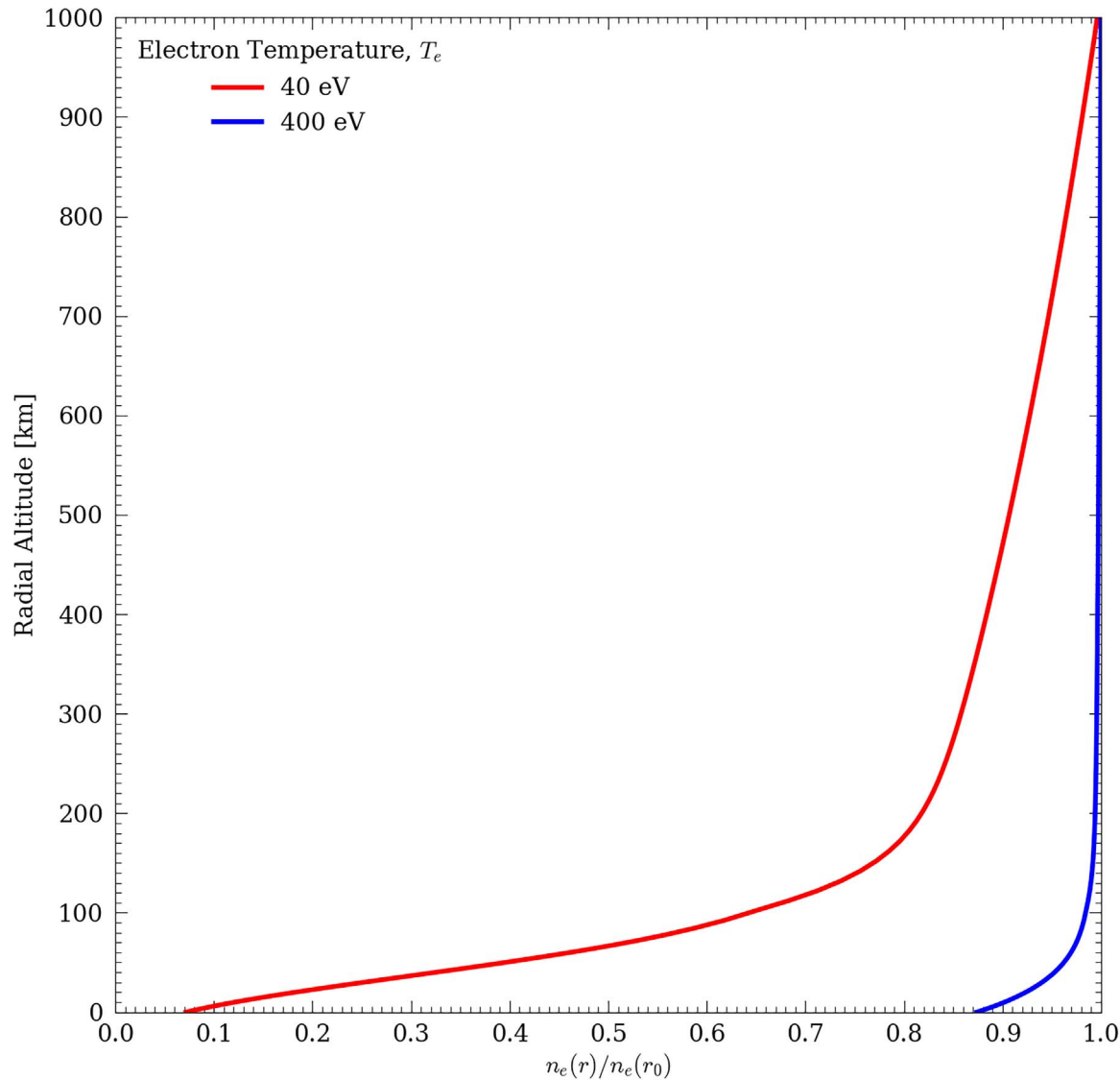


Figure B2. The ratio of the number density of electrons that reach the surface without depositing all of their energy compared to the number density of electrons at the top of the atmosphere according to an initial temperature of 40 eV (red) and 400 eV (blue).

Appendix C Photochemical Reactions

Below, we list the several photochemical reactions (DR, ion–neutral chemistry) that are simulated in the model of Callisto’s ionosphere presented in this study (Tables C1–C19).

Note that several rates are taken from the publicly available University of Manchester Institute of Science and Technology Database for Astrochemistry (UDfA; T. J. Millar et al. 2024) and references therein.

Table C1
Dissociate Recombination Rates Implemented in the Photochemical Model of Callisto's Ionosphere as a Function of Ionospheric Electron Temperature, T_e , in Units of K

Reactants	Products	Rate ($\text{cm}^3 \text{s}^{-1}$)	Reference
$\text{H}^+ + e^-$	H	$6.06 \times 10^{-11} T_e^{-0.75}$	UDfA
$\text{H}_2^+ + e^-$	2H	$2.91 \times 10^{-7} T_e^{-0.43}$	H. Hus et al. (1988)
$\text{H}_3^+ + e^-$	$\text{H}_2 + \text{H}$	$4.05 \times 10^{-7} T_e^{-0.52}$	UDfA
	3H	$7.55 \times 10^{-8} T_e^{-0.52}$	
$\text{O}^+ + e^-$	O	$1.24 \times 10^{-10} T_e^{-0.63}$	
$\text{O}_2^+ + e^-$	2O	$1.06 \times 10^{-5} T_e^{-0.70}$	
$\text{OH}^+ + e^-$	$\text{O} + \text{H}$	$6.50 \times 10^{-7} T_e^{-0.50}$	
$\text{O}_2\text{H}^+ + e^-$	$\text{O}_2 + \text{H}$	$3.00 \times 10^{-7} T_e^{-0.50}$	
$\text{H}_2\text{O}^+ + e^-$	$\text{OH} + \text{H}$	$2.77 \times 10^{-6} T_e^{-0.50}$	
	$\text{O} + \text{H}_2$	$3.46 \times 10^{-6} T_e^{-0.50}$	
$\text{H}_3\text{O}^+ + e^-$	$\text{H}_2\text{O} + \text{H}$	$6.06 \times 10^{-6} T_e^{-0.50}$	
	OH + 2H	$1.13 \times 10^{-5} T_e^{-0.50}$	
$\text{HCO}^+ + e^-$	$\text{CO} + \text{H}$	$1.23 \times 10^{-5} T_e^{-0.69}$	C. R. Herd et al. (1990)
$\text{HCO}_2^+ + e^-$	$\text{OH} + \text{CO}$	$1.91 \times 10^{-6} T_e^{-0.50}$	V. A. Krasnopolsky (2002)
	$\text{CO}_2 + \text{H}$	$5.89 \times 10^{-6} T_e^{-0.50}$	
$\text{C}^+ + e^-$	C	$1.91 \times 10^{-10} T_e^{-0.70}$	Y. H. Kim & J. L. Fox (1994)
$\text{CO}^+ + e^-$	O + C	$1.38 \times 10^{-6} T_e^{-0.46}$	UDfA
$\text{CO}_2^+ + e^-$	O + CO	$6.58 \times 10^{-6} T_e^{-0.50}$	

Table C2
Dissociate Recombination Rates Implemented in the Photochemical Model of Callisto's Ionosphere as a Function of Ionospheric Electron Temperature, T_e

Reactants	Products	Rate ($\text{cm}^3 \text{s}^{-1}$)	Reference
$\text{CH}^+ + e^-$	C + H	$1.65 \times 10^{-6} T_e^{-0.42}$	Y. H. Kim & J. L. Fox (1994)
$\text{CH}_2^+ + e^-$	$\text{CH} + \text{H}$	$4.33 \times 10^{-6} T_e^{-0.50}$	
$\text{CH}_3^+ + e^-$	$\text{CH}_2 + \text{H}$	$6.06 \times 10^{-6} T_e^{-0.50}$	
$\text{CH}_4^+ + e^-$	$\text{CH}_3 + \text{H}$	$3.03 \times 10^{-6} T_e^{-0.50}$	
	$\text{CH}_2 + 2\text{H}$	$3.03 \times 10^{-6} T_e^{-0.50}$	
$\text{CH}_5^+ + e^-$	$\text{CH}_2 + \text{H}_2 + \text{H}$	$1.52 \times 10^{-5} T_e^{-0.50}$	
	$\text{CH}_3 + 2\text{H}$	$3.81 \times 10^{-6} T_e^{-0.50}$	
$\text{HOC}^+ + e^-$	$\text{CO} + \text{H}$	$3.30 \times 10^{-5} T_e^{-1.00}$	H. Liszt et al. (2004)

Note. Note that while these reactions are actually considered in the model, the densities of these species are negligible and thus not included in any of the plots presented.

Table C3
Ion–Neutral Chemical Rates Involving H^+ as a Reactant Implemented in the Photochemical Model of Callisto's Ionosphere

Reactants	Products	Rate ($\text{cm}^3 \text{s}^{-1}$)	Reference
$\text{H}^+ + \text{H}_2$	$\text{H}_3^+ + h\nu$	1.30×10^{-16}	V. Vuitton et al. (2007)
$\text{H}^+ + \text{O}$	$\text{O}^+ + \text{H}$	3.75×10^{-10}	V. G. Anicich (1993)
$\text{H}^+ + \text{O}_2$	$\text{O}_2^+ + \text{H}$	2.00×10^{-9}	UDfA
$\text{H}^+ + \text{CO}_2$	$\text{HCO}^+ + \text{O}$	3.80×10^{-9}	V. G. Anicich (1993)

Table C4
Ion–Neutral Chemical Rates Involving H_2^+ as a Reactant Implemented in the Photochemical Model of Callisto’s Ionosphere

Reaction		Rate ($\text{cm}^3 \text{s}^{-1}$)	Reference
Reactants	Products		
$\text{H}_2^+ + \text{H}$	$\text{H}^+ + \text{H}_2$	6.40×10^{-10}	V. Vuillon et al. (2007)
$\text{H}_2^+ + \text{H}_2$	$\text{H}_3^+ + \text{H}$	2.00×10^{-9}	
$\text{H}_2^+ + \text{O}$	$\text{OH}^+ + \text{H}$	1.50×10^{-9}	UDfA
$\text{H}_2^+ + \text{O}_2$	$\text{O}_2^+ + \text{H}_2$	8.00×10^{-10}	
	$\text{O}_2\text{H}^+ + \text{H}$	1.90×10^{-9}	
$\text{H}_2^+ + \text{CO}$	$\text{HCO}^+ + \text{H}$	2.23×10^{-9}	V. G. Anicich (1993)
	$\text{CO}^+ + \text{H}_2$	6.44×10^{-10}	V. G. Anicich & W. T. Huntress (1986)
$\text{H}_2^+ + \text{CO}_2$	$\text{HCO}_2^+ + \text{H}$	2.35×10^{-9}	

Table C5
Ion–Neutral Chemical Rates Involving H_3^+ as a Reactant Implemented in the Photochemical Model of Callisto’s Ionosphere

Reaction		Rate ($\text{cm}^3 \text{s}^{-1}$)	Reference
Reactants	Products		
$\text{H}_3^+ + \text{O}$	$\text{OH}^+ + \text{H}_2$	4.00×10^{-10}	V. G. Anicich (1993)
	$\text{H}_2\text{O}^+ + \text{H}$	4.00×10^{-10}	
$\text{H}_3^+ + \text{O}_2$	$\text{O}_2\text{H}^+ + \text{H}_2$	9.30×10^{-10}	UDfA
$\text{H}_3^+ + \text{CO}$	$\text{HCO}^+ + \text{H}_2$	1.70×10^{-9}	V. G. Anicich (1993)
	$\text{HOC}^+ + \text{H}_2$	2.70×10^{-11}	J. K. Kim et al. (1975)
$\text{H}_3^+ + \text{CO}_2$	$\text{HCO}_2^+ + \text{H}_2$	2.00×10^{-9}	V. G. Anicich & W. T. Huntress (1986)

Table C8
Ion–Neutral Chemical Rates Involving O^+ as a Reactant Implemented in the Photochemical Model of Callisto’s Ionosphere

Reaction		Rate ($\text{cm}^3 \text{s}^{-1}$)	Reference
Reactants	Products		
$\text{O}^+ + \text{H}$	$\text{H}^+ + \text{O}$	6.40×10^{-10}	V. G. Anicich (1993)
$\text{O}^+ + \text{H}_2$	$\text{OH}^+ + \text{H}$	1.62×10^{-9}	
$\text{O}^+ + \text{O}_2$	$\text{O}_2^+ + \text{O}$	2.10×10^{-11}	R. Schunk & A. Nagy (2009)
$\text{O}^+ + \text{CO}$	$\text{CO}^+ + \text{O}$	4.90×10^{-12}	UDfA
$\text{O}^+ + \text{CO}_2$	$\text{O}_2^+ + \text{CO}$	1.10×10^{-9}	R. Schunk & A. Nagy (2009)

Table C6
Ion–Neutral Chemical Rates Involving H_2O^+ as a Reactant Implemented in the Photochemical Model of Callisto’s Ionosphere

Reaction		Rate ($\text{cm}^3 \text{s}^{-1}$)	Reference
Reactants	Products		
$\text{H}_2\text{O}^+ + \text{H}_2$	$\text{H}_3\text{O}^+ + \text{H}$	6.40×10^{-10}	UDfA
$\text{H}_2\text{O}^+ + \text{O}$	$\text{O}_2^+ + \text{H}_2$	4.00×10^{-11}	
$\text{H}_2\text{O}^+ + \text{O}_2$	$\text{O}_2^+ + \text{H}_2\text{O}$	4.60×10^{-10}	
$\text{H}_2\text{O}^+ + \text{CO}$	$\text{HCO}^+ + \text{OH}$	5.00×10^{-10}	

Table C7
Ion–Neutral Chemical Rates Involving HCO_2^+ as a Reactant Implemented in the Photochemical Model of Callisto’s Ionosphere

Reaction		Rate ($\text{cm}^3 \text{s}^{-1}$)	Reference
Reactants	Products		
$\text{HCO}_2^+ + \text{O}$	$\text{HCO}^+ + \text{O}_2$	1.00×10^{-9}	UDfA
$\text{HCO}_2^+ + \text{CO}$	$\text{HCO}^+ + \text{CO}_2$	7.80×10^{-10}	

Table C9
Ion–Neutral Chemical Rates Involving OH^+ as a Reactant Implemented in the Photochemical Model of Callisto’s Ionosphere

Reaction		Rate ($\text{cm}^3 \text{s}^{-1}$)	Reference
Reactants	Products		
$\text{OH}^+ + \text{H}_2$	$\text{H}_2\text{O}^+ + \text{H}$	9.70×10^{-10}	V. G. Anicich (1993)
$\text{OH}^+ + \text{O}$	$\text{O}_2^+ + \text{H}$	7.10×10^{-10}	
$\text{OH}^+ + \text{O}_2$	$\text{O}_2^+ + \text{OH}$	5.90×10^{-10}	UDfA
$\text{OH}^+ + \text{CO}$	$\text{HCO}^+ + \text{O}$	8.40×10^{-10}	V. G. Anicich (1993)
$\text{OH}^+ + \text{CO}_2$	$\text{HCO}_2^+ + \text{O}$	1.10×10^{-9}	

Table C10
Ion–Neutral Chemical Rates Involving O_2H^+ as a Reactant Implemented in the Photochemical Model of Callisto’s Ionosphere

Reaction		Rate ($\text{cm}^3 \text{s}^{-1}$)	Reference
Reactants	Products		
$\text{O}_2\text{H}^+ + \text{H}_2$	$\text{H}_3^+ + \text{O}_2$	6.40×10^{-10}	UDfA
$\text{O}_2\text{H}^+ + \text{O}$	$\text{OH}^+ + \text{O}_2$	6.20×10^{-10}	
$\text{O}_2\text{H}^+ + \text{O}_2$	$\text{HCO}^+ + \text{O}_2$	8.40×10^{-10}	
$\text{O}_2\text{H}^+ + \text{CO}_2$	$\text{HCO}_2^+ + \text{O}_2$	1.10×10^{-9}	

Table C11
Ion–Neutral Chemical Rates Involving C^+ as a Reactant Implemented in the Photochemical Model of Callisto’s Ionosphere

Reaction		Rate ($\text{cm}^3 \text{s}^{-1}$)	Reference
Reactants	Products		
$\text{C}^+ + \text{H}_2$	$\text{CH}^+ + \text{H}$	1.20×10^{-16}	J. K. Kim et al. (1975)
$\text{C}^+ + \text{O}$	$\text{CO}^+ + h\nu$	3.14×10^{-18}	UDfA
$\text{C}^+ + \text{O}_2$	$\text{CO}^+ + \text{O}$	3.42×10^{-10}	
	$\text{O}^+ + \text{CO}$	4.54×10^{-10}	
$\text{C}^+ + \text{CO}_2$	$\text{CO}^+ + \text{CO}$	1.10×10^{-9}	

Table C12
Ion–Neutral Chemical Rates Involving CO^+ as a Reactant Implemented in the Photochemical Model of Callisto’s Ionosphere

Reaction		Rate ($\text{cm}^3 \text{s}^{-1}$)	Reference
Reactants	Products		
$\text{CO}^+ + \text{H}$	$\text{H}^+ + \text{CO}$	7.50×10^{-10}	V. G. Anicich (1993)
$\text{CO}^+ + \text{H}_2$	$\text{HCO}^+ + \text{H}$	1.40×10^{-9}	
$\text{CO}^+ + \text{O}$	$\text{O}^+ + \text{CO}$	1.40×10^{-10}	
$\text{CO}^+ + \text{O}_2$	$\text{O}_2^+ + \text{CO}$	1.20×10^{-10}	UDfA
$\text{CO}^+ + \text{CO}_2$	$\text{CO}_2^+ + \text{CO}$	1.10×10^{-9}	V. G. Anicich (1993)

Table C13
Ion–Neutral Chemical Rates Involving CO_2^+ as a Reactant Implemented in the Photochemical Model of Callisto’s Ionosphere

Reaction		Rate ($\text{cm}^3 \text{s}^{-1}$)	Reference
Reactants	Products		
$\text{CO}_2^+ + \text{H}$	$\text{H}^+ + \text{CO}_2$	5.53×10^{-11}	V. G. Anicich (1993)
	$\text{HCO}^+ + \text{O}$	2.70×10^{-10}	
$\text{CO}_2^+ + \text{H}_2$	$\text{HCO}_2^+ + \text{H}$	8.70×10^{-10}	G. B. Scott et al. (1997)
$\text{CO}_2^+ + \text{O}$	$\text{O}^+ + \text{CO}_2$	9.62×10^{-11}	V. G. Anicich (1993)
	$\text{O}_2^+ + \text{CO}$	1.64×10^{-10}	
$\text{CO}_2^+ + \text{O}_2$	$\text{O}_2^+ + \text{CO}_2$	5.30×10^{-11}	UDfA

Table C14
Ion–Neutral Chemical Rates Involving CH^+ as a Reactant Implemented in the Photochemical Model of Callisto’s Ionosphere

Reaction		Rate ($\text{cm}^3 \text{s}^{-1}$)	Reference
Reactants	Products		
$\text{CH}^+ + \text{H}$	$\text{C}^+ + \text{H}_2$	7.50×10^{-10}	V. Vuitton et al. (2007)
$\text{CH}^+ + \text{H}_2$	$\text{CH}_2^+ + \text{H}$	1.20×10^{-9}	
$\text{CH}^+ + \text{O}$	$\text{H}^+ + \text{CO}$	1.75×10^{-11}	V. G. Anicich (1993)
	$\text{CO}^+ + \text{H}$	1.75×10^{-11}	
$\text{CH}^+ + \text{O}_2$	$\text{CO}^+ + \text{OH}$	1.00×10^{-11}	UDfA
	$\text{HCO}^+ + \text{O}$	9.70×10^{-10}	
	$\text{O}^+ + \text{HCO}$	1.00×10^{-11}	
$\text{CH}^+ + \text{CO}$	$\text{HCO}^+ + \text{C}$	7.00×10^{-12}	V. G. Anicich (1993)
$\text{CH}^+ + \text{CO}_2$	$\text{HCO}^+ + \text{CO}$	1.60×10^{-9}	UDfA

Table C15
Ion–Neutral Chemical Rates Involving CH_2^+ as a Reactant Implemented in the Photochemical Model of Callisto’s Ionosphere

Reaction		Rate ($\text{cm}^3 \text{s}^{-1}$)	Reference
Reactants	Products		
$\text{CH}_2^+ + \text{H}$	$\text{CH}^+ + \text{H}_2$	1.00×10^{-20}	UDfA
$\text{CH}_2^+ + \text{H}_2$	$\text{CH}_3^+ + \text{H}$	1.16×10^{-9}	V. Vuitton et al. (2007)
$\text{CH}_2^+ + \text{O}_2$	$\text{HCO}^+ + \text{OH}$	9.10×10^{-10}	UDfA
$\text{CH}_2^+ + \text{CO}_2$	$\text{H}_2\text{CO}^+ + \text{CO}$	1.60×10^{-9}	

Table C16
Ion–Neutral Chemical Rates Involving CH_3^+ as a Reactant Implemented in the Photochemical Model of Callisto’s Ionosphere

Reaction		Rate ($\text{cm}^3 \text{s}^{-1}$)	Reference
Reactants	Products		
$\text{CH}_3^+ + \text{H}$	$\text{CH}_2^+ + \text{H}_2$	3.61×10^{-33}	UDfA
$\text{CH}_3^+ + \text{O}$	$\text{H}_3^+ + \text{CO}$	2.20×10^{-10}	J. K. Kim et al. (1975)
	$\text{HCO}^+ + \text{H}_2$	2.20×10^{-10}	
$\text{CH}_3^+ + \text{O}_2$	$\text{H}_3\text{CO}^+ + \text{O}$	5.00×10^{-12}	UDfA

Table C17
Ion–Neutral Chemical Rates Involving CH_4^+ as a Reactant Implemented in the Photochemical Model of Callisto’s Ionosphere

Reaction		Rate ($\text{cm}^3 \text{s}^{-1}$)	Reference
Reactants	Products		
$\text{CH}_4^+ + \text{H}$	$\text{CH}_3^+ + \text{H}_2$	1.00×10^{-11}	UDfA
$\text{CH}_4^+ + \text{H}_2$	$\text{CH}_5^+ + \text{H}$	3.50×10^{-11}	V. Vuitton et al. (2007)
$\text{CH}_4^+ + \text{O}_2$	$\text{O}_2^+ + \text{CH}_4$	3.90×10^{-10}	UDfA
$\text{CH}_4^+ + \text{CO}$	$\text{HCO}^+ + \text{CH}_3$	1.04×10^{-9}	V. G. Anicich (1993)
$\text{CH}_4^+ + \text{CO}_2$	$\text{HCO}_2^+ + \text{CH}_3$	1.20×10^{-9}	UDfA

Table C18
Ion–Neutral Chemical Rates Involving CH_5^+ as a Reactant Implemented in the Photochemical Model of Callisto’s Ionosphere

Reaction		Rate ($\text{cm}^3 \text{s}^{-1}$)	Reference
Reactants	Products		
$\text{CH}_5^+ + \text{H}$	$\text{CH}_4^+ + \text{H}_2$	1.50×10^{-10}	V. Vuitton et al. (2007)
$\text{CH}_5^+ + \text{O}$	$\text{H}_3\text{O}^+ + \text{CH}_2$	3.70×10^{-9}	V. G. Anicich (1993)
$\text{CH}_5^+ + \text{CO}$	$\text{HCO}^+ + \text{CH}_4$	9.90×10^{-10}	
$\text{CH}_5^+ + \text{CO}_2$	$\text{HCO}_2^+ + \text{CH}_4$	3.20×10^{-11}	UDfA

Table C19
Ion–Neutral Chemical Rates Involving HOC^+ as a Reactant Implemented in the Photochemical Model of Callisto’s Ionosphere

Reaction		Rate ($\text{cm}^3 \text{s}^{-1}$)	Reference
Reactants	Products		
$\text{HOC}^+ + \text{H}_2$	$\text{H}_3^+ + \text{CO}$	2.35×10^{-10}	V. G. Anicich (1993)
	$\text{HCO}^+ + \text{H}_2$	2.35×10^{-10}	
$\text{HOC}^+ + \text{CO}$	$\text{HCO}^+ + \text{CO}$	6.00×10^{-10}	
$\text{HOC}^+ + \text{CO}_2$	$\text{HCO}_2^+ + \text{CO}$	9.00×10^{-10}	

Appendix D

Callisto's Ionosphere Sourced by Photo- and Magnetospheric Electron-impact Ionization

Figures D1 and D2 illustrate the ion density profiles from the photochemical models carried out in this study, where interactions with photons and magnetospheric electrons were

considered. In these models, at the top of the atmosphere, the latter was assumed to have a density of $n_e = 1 \text{ cm}^{-3}$ and a temperature of either $T_e = 40 \text{ eV}$ (Figure D1) or $T_e = 400 \text{ eV}$ (Figure D2). As in Figure 4, we compare these results to the Juice/PEP/NIM detection threshold above the spacecraft's C/A altitude.

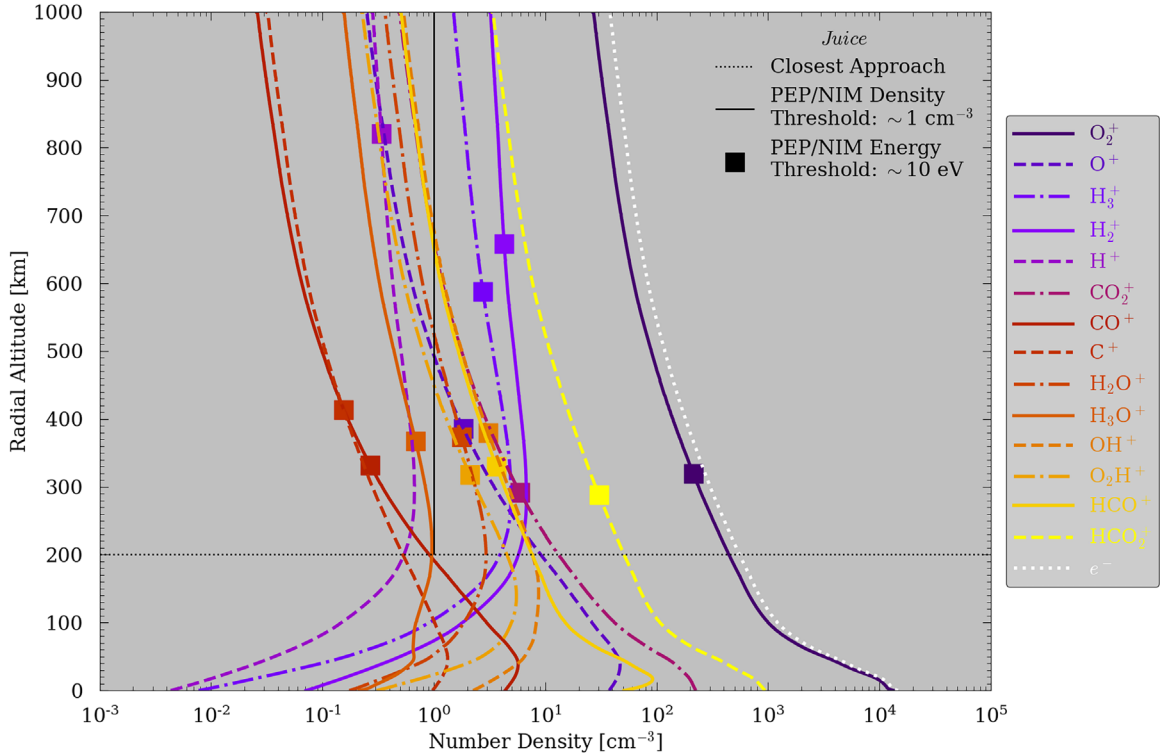


Figure D1. Results from photochemical models of Callisto's ionosphere, with inputs taken from DSMC models of Callisto's neutral atmosphere (Figure 3), which is ionized by interactions with photons and magnetospheric electrons with a number density of 1 cm^{-3} and a temperature of 40 eV at the top of the atmosphere. We also list the expected Juice C/A altitude (200 km) as well as the density and energy thresholds for its PEP/NIM instrument, $\sim 1 \text{ cm}^{-3}$ and 10 eV , respectively.

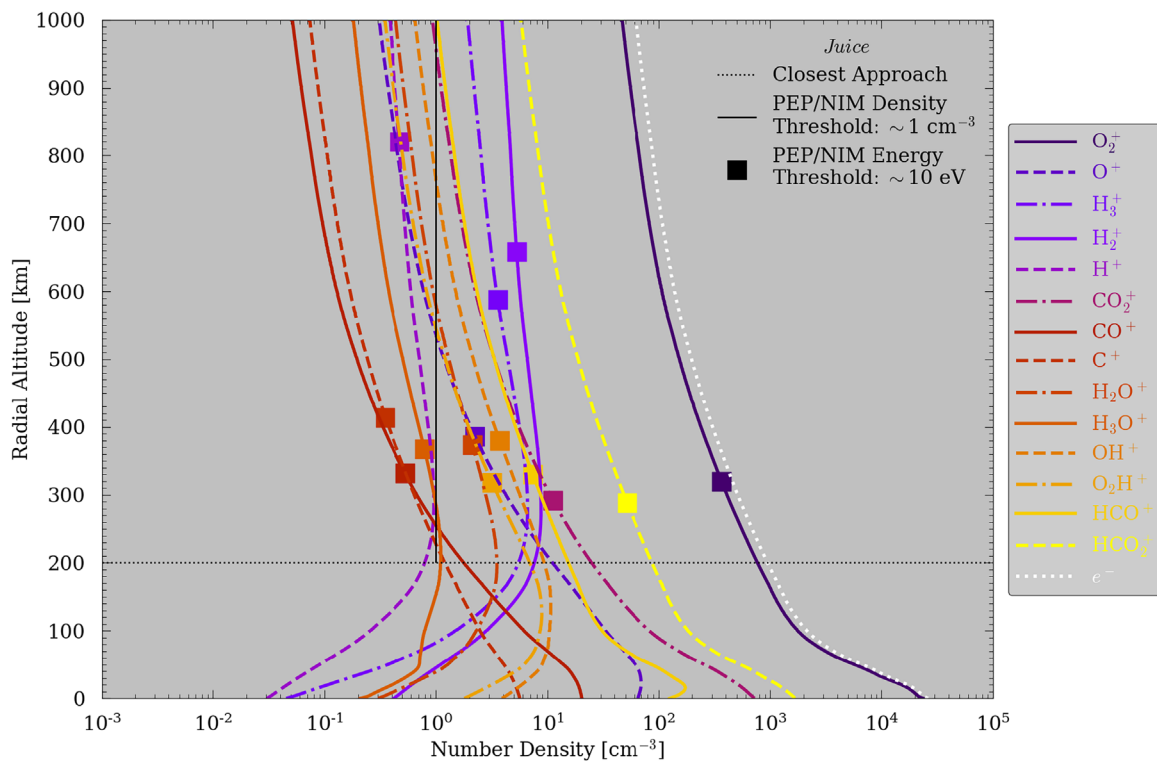


Figure D2. Results from photochemical models of Callisto's ionosphere, with inputs taken from DSMC models of Callisto's neutral atmosphere (Figure 3), which is ionized by interactions with photons and magnetospheric electrons with a number density of 1 cm^{-3} and a temperature of 400 eV at the top of the atmosphere. We also list the expected Juice C/A altitude (200 km) as well as the density and energy thresholds for its PEP/NIM instrument, $\sim 1 \text{ cm}^{-3}$ and 10 eV, respectively.

ORCID iDs

- Shane R. Carberry Mogan <https://orcid.org/0000-0002-0261-8117>
 Luke E. Moore <https://orcid.org/0000-0003-4481-9862>
 Lucas Liuzzo <https://orcid.org/0000-0002-4820-8594>
 Andrew R. Poppe <https://orcid.org/0000-0001-8137-8176>

References

- Anicich, V. G. 1993, Evaluated Bimolecular Ion-molecule Gas Phase Kinetics of Positive Ions for Use in Modeling Planetary Atmospheres, Cometary Comae, and Interstellar Clouds, *JPCRD*, **22**, 1469
 Anicich, V. G., & Huntress, W. T. 1986, A Survey of Bimolecular Ion-molecule Reactions for Use in Modeling the Chemistry of Planetary Atmospheres, Cometary Comae, and Interstellar Clouds, *ApJS*, **62**, 553
 Barth, C. A., Hord, C. W., Stewart, A. I. F., et al. 1997, Galileo Ultraviolet Spectrometer Observations of Atomic Hydrogen in the Atmosphere of Ganymede, *GeoRL*, **24**, 2147
 Bird, G. A. 1994, Molecular Gas Dynamics and the Direct Simulation of Gas Flows. Molecular Gas Dynamics and the Direct Simulation of Gas Flows (Oxford: Oxford Univ. Press)
 Bockelée-Morvan, D., Poch, O., Leblanc, F., et al. 2024, A Patchy CO_2 Exosphere on Ganymede Revealed by the James Webb Space Telescope, *A&A*, **690**, L11
 Brinkmann, R. T. 1970, Departures from Jeans' Escape Rate for H and He in The Earth's Atmosphere, *P&SS*, **18**, 449
 Broadfoot, A. L., Belton, M. J. S., Takacs, P. Z., et al. 1979, Extreme Ultraviolet Observations from Voyager 1 Encounter with Jupiter, *Sci*, **204**, 979
 Carberry Mogan, S. R., Johnson, R. E., Vorburger, A., & Roth, L. 2023a, Electron Impact Ionization in the Icy Galilean Satellites' Atmospheres, *EPJD*, **77**, 26
 Carberry Mogan, S. R., Liuzzo, L. L., & Poppe, A. R. 2024, The Influence of Non-thermal Collisions in Europa's Atmosphere, *GeoRL*, **51**, e2024GL109534
 Carberry Mogan, S. R., Liuzzo, L., Poppe, A. R., et al. 2023b, Callisto's Atmosphere: The Oxygen Enigma, *JGRE*, **128**, e2023JE007894
 Carberry Mogan, S. R., Tucker, O. J., & Johnson, R. E. 2021a, The Influence of Upper Boundary Conditions on Molecular Kinetic Atmospheric Escape Simulations, *P&SS*, **205**, 105302
 Carberry Mogan, S. R., Tucker, O. J., Johnson, R. E., et al. 2020, The Influence of Collisions and Thermal Escape in Callisto's Atmosphere, *Icar*, **352**, 113932
 Carberry Mogan, S. R., Tucker, O. J., Johnson, R. E., et al. 2021b, A Tenuous, Collisional Atmosphere on Callisto, *Icar*, **368**, 114597
 Carberry Mogan, S. R., Tucker, O. J., Johnson, R. E., et al. 2022, Callisto's Atmosphere: First Evidence for H_2 and Constraints on H_2O , *JGRE*, **127**, e2022JE007294
 Carlson, R. W. 1999, A Tenuous Carbon Dioxide Atmosphere on Jupiter's Moon Callisto, *Sci*, **283**, 820
 Cartwright, R. J., Villanueva, G. L., Holler, B. J., et al. 2024, Revealing Callisto's Carbon-rich Surface and CO_2 Atmosphere with JWST, *PSJ*, **5**, 60
 Cosby, P. C. 1993, Electron-impact Dissociation of Oxygen, *JChPh*, **98**, 9560
 Cunningham, N. J., Spencer, J. R., Feldman, P. D., et al. 2015, Detection of Callisto's Oxygen Atmosphere with the Hubble Space Telescope, *Icar*, **254**, 178
 de Kleer, K., Milby, Z., Schmidt, C., et al. 2023, The Optical Aurorae of Europa, Ganymede, and Callisto, *PSJ*, **4**, 37
 Duling, S., Saur, J., Clark, G., et al. 2022, Ganymede MHD Model: Magnetospheric Context for Juno's PJ34 Flyby, *GeoRL*, **49**, e2022GL101688
 Galand, M., Moore, L., Charnay, B., et al. 2009, Solar Primary and Secondary Ionization at Saturn, *JGRE*, **114**, A06313
 Galli, A., Vorburger, A., Carberry Mogan, S. R., et al. 2022, Callisto's Atmosphere and Its Space Environment: Prospects for the Particle Environment Package on Board JUICE, *E&SS*, **9**, e02172
 Gurnett, D. A., Kurth, W. S., Roux, A., & Bolton, S. J. 1997, Absence of a Magnetic-field Signature in Plasma-wave Observations at Callisto, *Natur*, **387**, 261
 Gurnett, D. A., Persoon, A. M., Kurth, W. S., et al. 2000, Plasma Densities in the Vicinity of Callisto from Galileo Plasma Wave Observations, *GeoRL*, **27**, 1867
 Hartkorn, O., Saur, J., & Strobel, D. F. 2017, Structure and Density of Callisto's Atmosphere from a Fluid-kinetic Model of Its Ionosphere: Comparison with Hubble Space Telescope and Galileo Observations, *Icar*, **282**, 237

- Haynes, C. M., Tippens, T., Addison, P., et al. 2023, Emission of Energetic Neutral Atoms from the Magnetosphere-atmosphere Interactions at Callisto and Europa, *JGRE*, **128**, e2023JA031931
- Haynes, C. M., Tippens, T., Simon, S., & Liuzzo, L. 2025, Constraints on the Observability of Energetic Neutral Atoms from the Magnetosphere-atmosphere Interactions at Callisto and Europa, *JGRA*, **130**, e2024JA033391
- Herd, C. R., Adams, N. G., & Smith, D. 1990, OH Production in the Dissociative Recombination of H_3O^+ , HCO_2^+ , and N_2OH^+ -Comparison with Theory and Interstellar Implications, *ApJ*, **349**, 388
- Huebner, W. F., & Mukherjee, J. 2015, Photoionization and Photodissociation Rates in Solar and Blackbody Radiation Fields, *P&SS*, **106**, 11
- Hus, H., Yousif, F., Noren, C., et al. 1988, Dissociative Recombination of Electrons with H_2^+ in Low Vibrational States, *PhRvL*, **60**, 1006
- Itikawa, Y. 2002, Cross Sections for Electron Collisions with Carbon Dioxide, *JPCRD*, **31**, 749
- Itikawa, Y. 2015, Cross Sections for Electron Collisions with Carbon Monoxide, *JPCRD*, **44**, 013105
- Itikawa, Y., & Mason, N. 2005, Cross Sections for Electron Collisions with Water Molecules, *JPCRD*, **34**, 1
- Johnson, R. E. 1990, Energetic Charged-particle Interactions with Atmospheres and Surfaces (Berlin: Springer)
- Kim, J. K., Theard, L. P., & Huntress, W. T., Jr. 1975, Proton Transfer Reactions from H_3^+ Ions to N_2 , O_2 , and CO Molecules, *CPL*, **32**, 610
- Kim, T. K., Ebert, R. W., Valek, P. W., et al. 2020, Survey of Ion Properties in Jupiter's Plasma Sheet: Juno JADE-I Observations, *JGRA*, **125**, e2019JA027696
- Kim, Y. H., & Fox, J. L. 1994, The Chemistry of Hydrocarbon Ions in the Jovian Ionosphere, *Icar*, **112**, 310
- Kivelson, M. G., Bagenal, F., Kurth, W. S., et al. 2004, Magnetospheric Interactions with Satellites, Jupiter: The Planet, Satellites and Magnetosphere (Cambridge: Cambridge Univ. Press), 513
- Kliore, A. J., Anabtawi, A., Herrera, R. G., et al. 2002, Ionosphere of Callisto from Galileo Radio Occultation Observations, *JGRA*, **107**, 1407
- Krasnopolksy, V. A. 2002, Mars' Upper Atmosphere and Ionosphere at Low, Medium, and High Solar Activities: Implications for Evolution of Water, *JGRE*, **107**, 5128
- Leblanc, F., Oza, A. V., Leclercq, L., et al. 2017, On the Orbital Variability of Ganymede's Atmosphere, *Icar*, **293**, 185
- Lewkow, N. R., & Kharchenko, V. 2014, Precipitation of Energetic Neutral Atoms and Induced Non-thermal Escape Fluxes from the Martian Atmosphere, *ApJ*, **790**, 98
- Liang, M.-C., Lane, B. F., Pappalardo, R. T., et al. 2005, Atmosphere of Callisto, *JGRE*, **110**, E02003
- Ligterink, N. F. W., Kipfer, K. A., & Gavino, S. 2024, Mind the Trap. Non-negligible Effect of Volatile Trapping in Ice on C/O Ratios in Protoplanetary Disks and Exoplanetary Atmospheres, *A&A*, **687**, A224
- Liszt, H., Lucas, R., & Black, J. H. 2004, The Abundance of + in Diffuse Clouds, *A&A*, **428**, 117
- Liuzzo, L., Feyerabend, M., Simon, S., & Motschmann, U. 2015, The Impact of Callisto's Atmosphere on Its Plasma Interaction with the Jovian Magnetosphere, *JGRA*, **120**, 9401
- Liuzzo, L., Poppe, A. R., Addison, P., et al. 2022, Energetic Magnetospheric Particle Fluxes onto Callisto's Atmosphere, *JGRA*, **127**, e2022JA030915
- Liuzzo, L., Poppe, A. R., Nénon, Q., Simon, S., & Addison, P. 2024, Constraining the Influence of Callisto's Perturbed Electromagnetic Environment on Energetic Particle Observations, *JGRA*, **129**, e2023JA032189
- Liuzzo, L., Simon, S., & Feyerabend, M. 2018, Observability of Callisto's Inductive Signature During the Jupiter Icy Moons Explorer Mission, *JGRA*, **123**, 9045
- Liuzzo, L., Simon, S., Feyerabend, M., & Motschmann, U. 2016, Disentangling Plasma Interaction and Induction Signatures at Callisto: The Galileo C10 Flyby, *JGRA*, **121**, 8677
- Liuzzo, L., Simon, S., Feyerabend, M., & Motschmann, U. 2017, Magnetic Signatures of Plasma Interaction and Induction at Callisto: The Galileo C21, C22, C23, and C30 Flybys, *JGRA*, **122**, 7364
- Liuzzo, L., Simon, S., & Regoli, L. 2019a, Energetic Electron Dynamics Near Callisto, *P&SS*, **179**, 104726
- Liuzzo, L., Simon, S., & Regoli, L. 2019b, Energetic Ion Dynamics Near Callisto, *P&SS*, **166**, 23
- Marconi, M. L. 2007, A Kinetic Model of Ganymede's Atmosphere, *Icar*, **190**, 155
- McComas, D. J., Alexander, N., Allegrini, F., et al. 2017, The Jovian Auroral Distributions Experiment (JADE) on the Juno Mission to Jupiter, *SSRv*, **213**, 547
- Millar, T. J., Walsh, C., Van de Sande, M., & Markwick, A. 2024, The UMIST Database for Astrochemistry 2022, *A&A*, **682**, A109
- Moore, L. E., Galand, M., Kliore, A. J., et al. 2018, Saturn's Ionosphere, Saturn in the 21st Century, Vol. 20 (Cambridge: Cambridge Univ. Press), 196
- Moore, L. E., Melin, H., O'Donoghue, J., et al. 2019, Modeling H_3^+ in Planetary Atmospheres: Effects of Vertical Gradients on Observed Quantities, *RSPTA*, **377**, 20190067
- Moore, L. E., Mendillo, M., Müller-Wodarg, I. C. F., & Murr, D. L. 2004, Modeling of Global Variations and Ring Shadowing in Saturn's Ionosphere, *Icar*, **172**, 503
- Neubauer, F. M. 1998, The Sub-Alfvénic Interaction of the Galilean Satellites with the Jovian Magnetosphere, *JGR*, **103**, 19843
- Roth, L., Alday, J., Becker, T. M., et al. 2017a, Detection of a Hydrogen Corona at Callisto, *JGRE*, **122**, 1046
- Roth, L., Carberry Mogan, S. R., Cartwright, R., et al. 2024, A UV Eclipse Test for Callisto's Atmosphere, Plasma Interaction and Water Ocean, HST Proposal, 17739
- Roth, L., Ivchenko, N., Gladstone, G. R., et al. 2021, A Sublimated Water Atmosphere on Ganymede Detected from Hubble Space Telescope Observations, *NatAs*, **5**, 1043
- Roth, L., Retherford, K. D., Ivchenko, N., et al. 2017b, Detection of a Hydrogen Corona in HST Ly α Images of Europa in Transit of Jupiter, *AJ*, **153**, 67
- Roth, L., Saur, J., Retherford, K. D., et al. 2016, Europa's Far Ultraviolet Oxygen Aurora from a Comprehensive Set of HST Observations, *JGRA*, **121**, 2143
- Roth, L., Smith, H. T., Yoshioka, K., et al. 2023, Constraints on Europa's Water Group Torus from HST/COS Observations, *PSJ*, **4**, 87
- Scarlett, L. H., Tapley, J. K., Fursa, D. V., et al. 2018, Electron-impact Dissociation of Molecular Hydrogen into Neutral Fragments, *EPJD*, **72**, 34
- Schunk, R., & Nagy, A. 2009, Ionospheres: Plasma Physics, and Chemistry (Cambridge: Cambridge Univ. Press)
- Scott, G. B., Fairley, D. A., Freeman, C. G., et al. 1997, Gas Phase Reactions of Some Positive Ions with Atomic and Molecular Hydrogen at 300 K, *JChPh*, **106**, 3982
- Sittler, E. C., & Strobel, D. F. 1987, Io Plasma Torus Electrons: Voyager 1, *JGR*, **92**, 5741
- Smith, G. R., Shemansky, D. E., Broadfoot, A. L., & Wallace, L. 1978, Monte Carlo Modeling of Exospheric Bodies: Mercury, *JGR*, **83**, 3783
- Smith, H. T., Mitchell, D. G., Johnson, R. E., et al. 2019, Europa Neutral Torus Confirmation and Characterization Based on Observations and Modeling, *ApJ*, **871**, 69
- Smyth, W. H., & Marconi, M. L. 2006, Europa's Atmosphere, Gas Tori, and Magnetospheric Implications, *Icar*, **181**, 510
- Straub, H. C., Renault, P., Lindsay, B. G., et al. 1996, ABsolute Partial Cross Sections for Electron-impact Ionization of H_2 , N_2 , and O_2 from Threshold to 1000 eV, *PhRVA*, **54**, 2146
- Strobel, D. F., Saur, J., Feldman, P. D., & McGrath, M. A. 2002, Hubble Space Telescope Space Telescope Imaging Spectrograph Search for an Atmosphere on Callisto: A Jovian Unipolar Inductor, *ApJL*, **581**, L51
- Szalay, J. R., Allegrini, F., Ebert, R. W., et al. 2024, Oxygen Production from Dissociation of Europa's Water-ice Surface, *NatAs*, **8**, 567
- Valek, P. W., Waite, J. H., Allegrini, F., et al. 2022, In Situ Ion Composition Observations of Ganymede's Outflowing Ionosphere, *GeoRL*, **49**, e2022GL100281
- Vorburger, A., Wurz, P., Lammer, H., et al. 2015, Monte-Carlo Simulation of Callisto's Exosphere, *Icar*, **262**, 14
- Vuitton, V., Yelle, R. V., & McEwan, M. J. 2007, Ion Chemistry and N-Containing Molecules in Titan's Upper Atmosphere, *Icar*, **191**, 722
- Waite, J. H., Jr., Greathouse, T. K., Carberry Mogan, S. R., et al. 2024, Magnetospheric-ionospheric-atmospheric Implications from the Juno Flyby of Ganymede, *JGRE*, **129**, e2023JE007859
- Woods, T. N., Eparvier, F. G., Bailey, S. M., et al. 2005, Solar EUV Experiment (SEE): Mission Overview and First Results, *JGRA*, **110**, A01312
- Yasuda, R., Kimura, T., Misawa, H., et al. 2024, Ray Tracing for Jupiter's Icy Moon Ionospheric Occultation of Jovian Auroral Radio Sources, *JGRA*, **129**, e2024JA032454